Fingerprints of order and disorder in the electronic and optical properties of crystalline and amorphous TiO_2

M. Landmann,[1] T. Köhler,[2] S. Köppen,[2] E. Rauls,[1] T. Frauenheim,[2] and W. G. Schmidt[1]
[1]*Lehrstuhl für Theoretische Physik, Universität Paderborn, 33095 Paderborn, Germany*
[2]*Bremen Center for Computational Materials Science, Universität Bremen, 28359 Bremen, Germany*
(Received 5 April 2012; published 6 August 2012)

We have investigated the structural and electronic properties as well as the linear optical response of amorphous TiO_2 within density functional theory and a numerically efficient density functional based tight-binding approach as well as many-body perturbation theory. The disordered TiO_2 phase is modeled by molecular dynamics. The equivalence to experimentally characterized amorphous phases is demonstrated by atomic structure factors and radial pair-distribution functions. By density functional theory calculations, using both the semilocal Perdew-Burke-Ernzerhof functional and the nonlocal Heyd-Scuseria-Ernzerhof screened hybrid functional, the electronic energy gap is found to be larger than in the crystalline TiO_2 phases rutile and brookite but close to the anatase band gap. The quasiparticle energy gap of amorphous TiO_2 is determined to be $\gtrsim$3.7 eV, while the optical gap is estimated to $\lesssim$3.5 eV. The disorder-induced formation of localized electronic states has been analyzed by the information entropy of the charge density distributions. The frequency-dependent optical constants, calculated from the complex dielectric function, have been determined in independent particle approximation. Besides similar absorption characteristics between the most common crystalline phases and amorphous TiO_2, we find distinct differences in the optical spectra in the energy region between 5 eV and 8 eV. These differences can be assigned to the loss of symmetry in the local atomic structure of the disordered material. While the composition of the crystalline phases rutile, anatase, and brookite is well described by periodic arrangements of distorted TiO_6 octahedra building blocks, the amorphous phase is characterized by partial loss of this octahedral coordination and the disorder-induced formation of under- and over-coordinated Ti ions. This leads to the absence of the characteristic crystal-field splitting of unoccupied Ti_{3d} states into e_g and t_{2g} like subbands. The optical characteristics of the amorphous phase are interpreted as a superposition of optical transitions that reflect the various local symmetries of the manifold of synthesizable crystalline TiO_2 phases. The linear optical properties, calculated within the independent-particle approximation, are found to be in good agreement with the available experimental data.

DOI: 10.1103/PhysRevB.86.064201 PACS number(s): 81.05.Gc, 71.23.Cq, 71.23.An

I. INTRODUCTION

TiO_2 shows an extended structure polymorphism, reflected in an extraordinary rich phase diagram. The three crystal types rutile [crystal system: tetragonal ($4/mmm$), space group: $P4_2/mnm$-D_{4h}^{14}], anatase [tetragonal ($4/mmm$), $I4_1/amd$-D_{4h}^{19}], and brookite [orthorhombic (mmm), $Pbca$-D_{2h}^{15}] are stable at atmospheric pressure and room temperature and commonly found in nature. A fourth naturally occurring phase TiO_2(B)[1,2] (monoclinic, bronze-type, $C2/m$) has been reported. Experiments have furthermore revealed the existence of the metastable oxides TiO_2(H)[3] (hollandite type, $I4/m$) and TiO_2(R)[4] (ramsdellite type, $Pbnm$), as well as the TiO_2 high-pressure polymorphs TiO_2(II)[5–7] [columbite type (α-PbO_2 structure), $Pbcn$], TiO_2(MI)[6–8] (monoclinic, baddeleyite type, $P2_1/c$), TiO_2(OI)[9] (orthohombic, $Pbca$), TiO_2(OII)[9,10] (orthohombic, cotunnite type, $Pnma$), and c-TiO_2[11,12] (cubic, fluorite type, $Fm3m$). From combined experimental and theoretical studies the phase-transition path rutile → columbite type [TiO_2(II)] → baddeleyite type [TiO_2(MI)] → intermediate orthorhombic type [TiO_2(OI)] → cotunnite type [TiO_2(OII)] has been identified for compression at ambient temperature.[9,13]

The structure of the three most common phases rutile, anatase, and brookite as well as the polymorphs TiO_2(B), TiO_2(R), TiO_2(H), and TiO_2(II) is well characterized in an edge-sharing octahedron-chain picture with single distorted TiO_6 octahedron building blocks formed by a central Ti ion surrounded by six O ions.[2,11,14–16] A complementary view of the electronic structure is given by crystal-lattice formation resting upon planar Ti_3O units.[17,18] Under pressure the coordination of the Ti ions and therefore the local atomic structure changes. TiO_2(MI) and TiO_2(OI) are characterized by a sevenfold coordination of Ti ions with O ions. In the cubic fluorite phase the Ti ions are eightfold coordinated, which results in the formation of tetrahedrally coordinated O ions. Finally, Ti ions in the high-pressure polymorph TiO_2(OII) are ninefold coordinated by O ions.

Besides this manifold of well-ordered TiO_2 modifications that are characterized by their ion's constant coordination number, also amorphous TiO_2 (a-TiO_2) has received interest as a low-cost material for technical applications, based on the extraordinary optical and catalytic properties known from the crystalline phases.[19,20] A graphical representation of a-TiO_2 is given in Fig. 1 using polyhedra to identify the TiO_x building blocks. a-TiO_2 is a general starting material (precursor) for the synthesis of various single-crystalline phases by hydrothermal treatment.[16,21–23] In practice a-TiO_2 is commonly produced in the form of thin films prepared by various experimental strategies as direct current (magnetron) sputtering,[24–28] electron-beam evaporation,[29,30] cathodic vacuum arc deposition,[31,32] sol-gel deposition,[33,34] reactive sputtering, and arc ion plating.[35,36] Also dense or porous disordered films of nanocrystallites are commonly

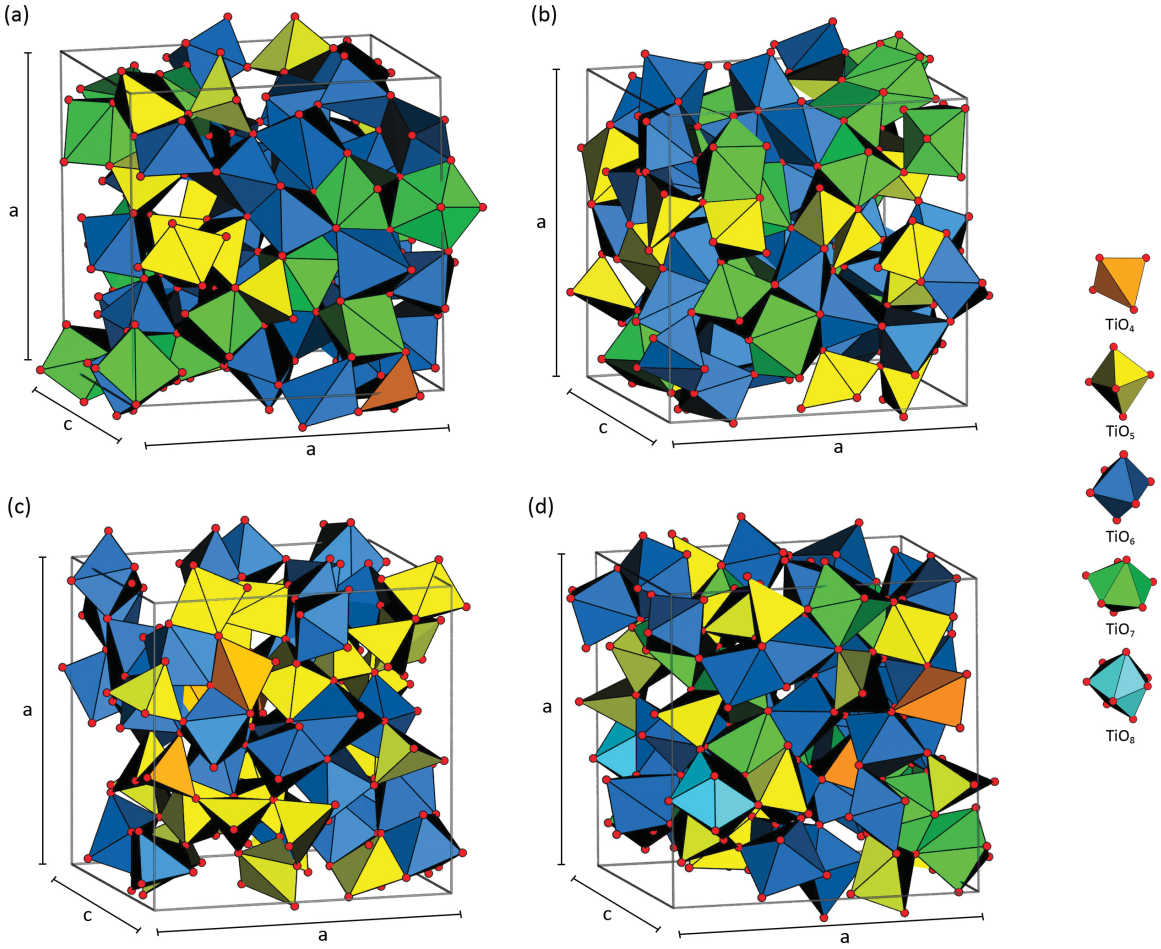

FIG. 1. (Color online) Polyhedra representation (2.5 Å Ti-O bond-length cutoff) of the TiO_x building blocks for the 216-atom rectangular cuboidal unit cells ($a = 13.80$ Å, $a = 11.93$ Å) of amorphous TiO_2 with a mass density of 4.20 g/cm^3. The structures on the left-hand side are room-temperature (300 K) structures generated by (a) CPMD and (c) DFTB based MD. On the right-hand side the geometry after structural relaxation with VASP is shown [(b) CPMD + VASP, (d) DFTB + VASP].

produced and referred to as amorphous films. Depending on the intended usage this might be a significant difference. A fundamental property of the amorphous material is the absence of optical anisotropies that, for instance, occur in the uniaxial rutile and anatase phases or the biaxial brookite phase. In addition, a pure amorphous phase is not influenced by grain boundary induced defects between the crystallites that modify the physical properties.[37,38] Closely related are size effects that might favor various crystalline phases in nanoparticulated TiO_2.[23,39–41] Also, it had been shown that a-TiO_2 films are well suited for surface passivation in bioimplant applications due to their high stability and corrosion resistance *in vitro*.[42,43]

While there is extended literature[13,44–62] on structural, elastic, thermodynamic, and optical/dielectric properties obtained from numerical simulations of the three most common crystalline phases as well as their low index surfaces,[63–70] computational data on a-TiO_2 are rather limited due to the necessity of using extended unit cells for an approximate numerical reproduction of amorphicity. In contrast to crystalline modifications, amorphous material phases stand out by their loss of translational symmetry/long-range order. Consequently, the theoretical tools developed mainly for crystalline materials cannot straightforwardly be applied to amorphous materials and their physical properties. An understanding of the formation of energy gaps and resulting optical properties in amorphous semiconductors is directly related to the question of whether the basic nature of electronic and optical properties depends on short-range order, i.e., localized electronic states, and/or long-range order, i.e., extended electronic states and well-defined energy bands.

Due to the early works of Anderson,[71,72] Cohen,[73] and Mott[74] on the electronic structure of disordered materials, a fundamental structural disorder induced localization of electronic states was realized. In contrast to the crystal, structural disorder induces under- and over-coordinated ions in the amorphous material phase. Such variations in the atomic and electronic structure are expected to cause localized states near the energy-gap edges, forming tails of occupied and unoccupied localized states that range into the forbidden energy region of the pure crystal phase. These tails (and the loss of momentum conservation) induce a HOMO-LUMO-type energy gap that deviates from the band gap defined for the crystal. The amorphous phase complement of the crystalline band gap, defined between valence and conduction band states, is called the "mobility gap" and defined as the energy difference between filled and empty nonlocalized extended

Bloch-type states. The mobility gap is always larger than the HOMO-LUMO-type gap and an important quantity with respect to the electrical properties, like the electron mobility and transport characteristics in amorphous solids in general.

To the best of our knowledge, no theoretical studies on the optical properties, in particular based on *ab initio* calculations, have been published for a-TiO_2 so far. A first density functional theory (DFT) study on the electronic structure of a-TiO_2 has been published recently.[75] The atomic structure of amorphous samples has been characterized in terms of distribution functions and structure factors by model calculations.[15,23,75,76] Petkov *et al.*[15] published a combined experimental and theoretical work on the structure of amorphous TiO_2. On the one hand, they fabricated thin films and bulk powder samples of a-TiO_2 that have been characterized by electron and x-ray diffraction. On the other hand, the experimental distribution functions have been compared to results of a reversed Monte Carlo (RMC) approach that optimizes a starting configuration to match the experimentally derived structure data. As a key result they reported a considerable resemblance of the atomic arrangement in their amorphous sample to the crystalline brookite phase. This observation has also been confirmed by molecular-dynamics (MD) simulations of Hoang[76] using empirical pair-interaction potentials. Therefore, it has been stated that there is a close relation between brookite and the amorphous phase of TiO_2. In addition, experimental results suggest brookite growth directly out of an amorphous phase. This has been demonstrated by brookite nanoparticles surrounded by an amorphous-like shell.[16] In contrast, predominantly phase transitions upon heating from a-TiO_2 films to anatase and partially to rutile are reported.[27,29,31,34–36] The difference in crystallization behavior of a-TiO_2 has been attributed to a strong dependence on the sample history as precursor chemistry, preparation method, and heat treatment.[16,77] Theoretically, the ratio of edge to vertex linked TiO_6 octahedral building blocks[15,76] has been found to play a major role in the crystallization behavior of a-TiO_2.

In this paper we will investigate the relevance of long-range order or rather its loss, thus extending our preceding study on crystalline TiO_2 polymorphs[17] to the structural, electronic, and optical properties to the amorphous phase of TiO_2. The paper is organized as follows: Section II describes the underlying theoretical molecular-dynamics (MD) frameworks needed to generate the amorphous material unit cells as well as the used numerical parameters to obtain the optical spectra within the DFT approach. Also, the information theory related concepts necessary to measure the degree of localization of electronic states are introduced. Section III is used for characterization of the amorphous structure and presenting the calculated electronic structure and optical spectra, which are discussed alongside existing experimental data. Finally, Sec. IV summarizes the relevant results and gives concluding comments and reasonings.

II. METHODOLOGY AND NUMERICAL DETAILS

DFT calculations[78,79] have been performed using the projector-augmented wave (PAW) method[80,81] as implemented in the Vienna *Ab initio* Simulation Package (VASP).[82] Both the generalized gradient approximation (GGA) according to Perdew-Burke-Ernzerhof (PBE)[83] as well as the nonlocal, range-separated, screened Coulomb potential hybrid density functional proposed by Heyd, Scuseria, and Ernzerhof (HSE06)[84–87] have been applied. Within the framework of many-body perturbation theory (MBPT),[88,89] quasiparticle (QP) corrections due to self-energy effects within the GW approximation have been included perturbatively in a full-frequency-dependent G_0W_0 scheme[90–93] (see also discussion in Ref. 94). Two-particle excitations are taken into account by solution of the Bethe-Salpeter equation (BSE) for Coulomb correlated (quasi)electrons and (quasi)holes.[95–98] To avoid the $O(N^3)$ scaling diagonalization of the electron-hole pair Hamiltonian, the calculation of the frequency-dependent dielectric function is performed by an $O(N^2)$ scaling time-evolution scheme.[99] A similar numerical setup has been applied to crystalline TiO_2 (see Ref. 17).

We additionally utilized the self-consistent charge density functional tight-binding (SCC-DFTB)[100–102] approach to the electronic structure of large-scale systems with the objective of generating and characterizing amorphous TiO_2 polymorphs by molecular dynamics. SCC-DFTB offers a good compromise between accuracy and computational efficiency and successfully addressed a wide range of material properties. We refer the reader to recent studies on diamond nucleation in amorphous carbon systems[103] or the discussion of the properties of exofluorinated carbon nanotubes,[104] as examples for either extended or low-dimensional systems of interest.

A. Modeling of amorphous materials

To model the structure formation in stoichiometric amorphous TiO_2 thin films, we performed MD simulated annealing (SA) calculations. On the one hand the SCC-DFTB scheme and on the other hand the *ab initio* Car-Parrinello molecular-dynamics (CPMD) method[105] were used. For the MD simulations we prepared initial structures containing 216 atoms, spatially and chemically randomly distributed, like a gas of hard spheres. The atoms are placed in a fixed-volume rectangular cuboidal supercell arrangement of a size matching the microscopic mass density of 4.20 g/cm^3 and the ideal 1:2 stoichiometry. For the present DFTB calculations we used the Ti-O interaction parametrization of Ref. 106. The dynamical quenching path for relaxation started from a partly equilibrated liquid state of the model structure at 5000 K and followed a path of exponentially decreasing temperature towards room temperature at 300 K. The total duration of the cooling procedure amounts 23 ps. The Newton's equations of motion are solved using the Verlet algorithm. The coupling to a heat bath, according to the canonical (*NVT*) ensemble, was realized by an Anderson thermostat.

The CPMD calculation was done under usage of norm-conserving pseudopotentials of Troullier-Martins type, proposed for Ti and O by Glassford *et al.*,[107,108] and application of the Becke88 exchange functional.[109] The total simulation time of 8.6 ps was discretized by 51 000 steps to ensure energy convergence. At the beginning and the end of the cooling process we performed thermal equilibration phases of 4000 steps at 5000 K and 5000 steps at room temperature 300 K,

respectively, and in between we followed an exponential like path approximated by a suitable stepwise function. Here the Nosé-Hoover thermostat ensures the conditions of a canonical ensemble and the volume was kept constant, too.

We additionally performed structural relaxations for both the DFTB and the CPMD room temperature structure using the the Vienna *Ab initio* Simulation Package (VASP).[82] The atomic positions have been relaxed using the PBE[83] (Perdew-Burke-Ernzerhof) functional, a $2 \times 2 \times 2$ Monkhorst-Pack k-point sampling, and a force convergence criterion of 0.01 eV/Å.

B. Characterization of amorphous materials

The characteristics of the remaining short-range order of amorphous materials can be characterized by a detailed analysis of the mean local bonding environment, describable in bond lengths and angle statistics as well as mean coordination numbers. All of that is typically expressed in terms of atomic structure factors and radial pair distribution functions (RDFs). If the total reduced atomic distribution function $G(r)$, directly accessible through numerical simulations, is defined through

$$G(r) = 4\pi r[\varrho(r) - \varrho_0] \tag{1}$$

with $\varrho(r)$ and ϱ_0 being the averaged atomic densities, both quantities are connected by a Fourier representation of the structure factor $S(q)$, respectively the reduced quantity $F(q) = q[S(q) - 1]$, according to

$$G(r) = \frac{2}{\pi}\int_0^\infty F(q)\sin(qr)dq, \tag{2}$$

where q is the the magnitude of the wave vector of the scattered photons/particles. The function $F(q)$ is also known as total reduced interference function.[110,111] The static atomic structure factor $S(q)$ is experimentally accessible by various diffraction techniques (electron, x ray, or neutron diffraction, depending on the type of the manufactured sample).

C. Numerical details

An energy cutoff of 400 eV was used and the $3s$ and $3p$ semicore states of Ti have been treated as valence states within the PAW potentials throughout this work. In agreement with the original definitions,[87,112] an exact exchange fraction of $\alpha = 0.25$ and a screening parameter of $\mu = 0.2$ Å^{-1} have been used in the HSE06 screened hybrid functional. The energy-loss function $L(\omega)$, the reflectivity $R(\omega)$, the refraction index $n(\omega)$, the extinction coefficient $\kappa(\omega)$, and the absorption coefficient $\alpha(\omega)$ have been calculated via

$$L(\omega) = \frac{\varepsilon_2(\omega)}{\varepsilon_1(\omega)^2 + \varepsilon_2(\omega)^2}, \tag{3}$$

$$R(\omega) = \left|\frac{\sqrt{\varepsilon_1(\omega) + i\varepsilon_2(\omega)} - 1}{\sqrt{\varepsilon_1(\omega) + i\varepsilon_2(\omega)} + 1}\right|^2, \tag{4}$$

$$n(\omega) = \frac{1}{\sqrt{2}}\sqrt{\varepsilon_1(\omega) + \sqrt{\varepsilon_1(\omega)^2 + \varepsilon_2(\omega)^2}}, \tag{5}$$

$$\kappa(\omega) = \frac{1}{\sqrt{2}}\sqrt{-\varepsilon_1(\omega) + \sqrt{\varepsilon_1(\omega)^2 + \varepsilon_2(\omega)^2}}, \tag{6}$$

$$\alpha(\omega) = \frac{\sqrt{2}\omega}{c}\sqrt{-\varepsilon_1(\omega) + \sqrt{\varepsilon_1(\omega)^2 + \varepsilon_2(\omega)^2}}, \tag{7}$$

from the frequency-dependent complex dielectric function $\varepsilon(\omega) = \varepsilon_1(\omega) + i\varepsilon_2(\omega)$ which is determined in independent particle approximation (IPA) [also termed random phase approximation (RPA)] by the Ehrenreich-Cohen formula[113] in the optical limit of vanishing wave vectors. The DFT energy gap underestimation has been corrected by a scissors shift approximation. The reliability and value of the applied scissors shift for the unoccupied energy bands in crystalline TiO_2 is discussed in Ref. 17. In the case of calculations for crystalline TiO_2 atomic positions and unit cells have been relaxed on the DFT-PBE level. Dielectric functions, the eigenvalue spectrum, and densities of states have been calculated for the relaxed unit cells using 28 electronic bands per formal TiO_2 unit. A $12 \times 12 \times 16$ Monkhorst-Pack k-point set for relaxation and 768 irreducible k points for determination of the dielectric properties have been applied for the rutile phase. For all other TiO_2 phases the k-point mesh has been adapted to reproduce a comparable point density in k space. DFT-PBE optical spectra of a-TiO_2 have been obtained for stoichiometric 216-atom orthorhombic unit cells ($a = 13.8046$ Å and $c = 11.9321$ Å; cf. Fig. 1) using 1920 electronic bands, a scissors shift of 1.3 eV, and a Γ-centered $3 \times 3 \times 3$ Monkhorst-Pack k-point mesh. The optical properties of four a-TiO_2 structure models, generated by DFTB and CPMD MD as well as additional structural relaxations by VASP, have been investigated on the DFT-IPA level of theory. Further numerical details and convergence considerations concerning the HSE06, G_0W_0, and BSE calculations are discussed in the text.

D. Analysis of electronic-state localization

The analysis of the disorder-induced localization of quantum states requires a measure to quantify the degree of localization. Information theory that unifies concepts from probability theory and statistics offers the necessary theoretical tools to determine this degree of localization, respectively the deviation from randomness. As expressed in the existence theorems of DFT, the information on the spatial extent of the individual electronic-state wave functions is bidirectionally unique contained in the corresponding charge density distributions. In the language of information theory, these electronic densities represent discrete, nonnegative N-point probability distributions that are in some way normalized to the number of electrons found in each electronic state and the number of sites used to represent the electron density.

In this study, we have investigated two measures to determine the degree of (de)localization of electronic states from their charge density distributions. Both measures are based on the generalized entropy concept of information theory. More precisely, both quantities are derived from the one-parametric continuous family of information entropies introduced by Alfréd Rényi.[114] For a finite discrete N-point probability distribution $\mathcal{P} = \{p_1, p_2 \ldots p_N\}$ with $\sum_{\nu=1}^{N} p_\nu = 1$, the Rényi entropy $H[\mathcal{P}] = H(p_1, p_2 \ldots p_N)$ of order α is

defined through

$$H_\alpha[\mathcal{P}] = \frac{1}{1-\alpha} \ln\left[\sum_{\nu=1}^{N} p_\nu^\alpha\right] \tag{8}$$

with $\alpha \geqslant 0$ and $\alpha \neq 1$. In the limit $\alpha \to 1$ this entropy definition tends to

$$H_1[\mathcal{P}] = \lim_{\alpha\to 1} H_\alpha[\mathcal{P}] = -\sum_{\nu=1}^{N} p_\nu \ln p_\nu. \tag{9}$$

Thus, the order-one Rényi entropy is identified as the information entropy introduced by Shannon.[114–117] The Rényi entropy of order two

$$H_2[\mathcal{P}] = -\ln\left[\sum_{\nu=1}^{N} p_\nu^2\right] \tag{10}$$

is known as extension entropy.[115] Both information and extension entropy provide a measures for the amount of uncertainty concerning the outcome of an *experiment* whose individual results are described by the probability distribution $\mathcal{P}$. In the same way, the entropies provide the amount of information that is obtained by carrying out the *experiment*. In analogy to the partition function of statistical thermodynamics and its relation to the entropy by the Boltzmann formula, the exponentiations $W[\mathcal{P}] = \exp\{H_1[\mathcal{P}]\}$ (Ref. 118) and $R[\mathcal{P}] = \exp\{H_2[\mathcal{P}]\}$ give the effective numbers of different outcomes, respectively the sum of accessible microstates in thermodynamic ensembles. The quantity $R[\mathcal{P}]$ is known as participation ratio (PR). Here, we will use the inverse quantities

$$W^{-1}[\mathcal{P}] = \exp\left\{\sum_{\nu=1}^{N} p_\nu \ln p_\nu\right\} \tag{11}$$

and

$$R^{-1}[\mathcal{P}] = \sum_{\nu=1}^{N} p_\nu^2 \tag{12}$$

to determine the degree of localization of electronic states in real space. $R^{-1}[\mathcal{P}]$ is commonly called the inverse participation ratio (IPR).[115,121–123]

Applied to the (partial) charge density distribution $\varrho_\nu(\mathbf{r})$ corresponding to a particular electronic state (respectively energy) ν, we obtain the degree of localization by

$$W^{-1}(\nu) = \exp\left\{\sum_{\mu=1}^{N} \varrho_\mu(\nu) \ln \varrho_\mu(\nu)\right\} \tag{13}$$

and

$$R^{-1}(\nu) = \sum_{\mu=1}^{N} [\varrho_\mu(\nu)]^2. \tag{14}$$

Here, μ describes the real-space grid points used to represent the charge density in the case of a plane wave representation of the Kohn-Sham eigenstate or the μ atom sites in the case of maximal localized basis states (i.e., Mulliken charge representation). According to the definitions above, higher values of $W^{-1}[\nu]$ and $R^{-1}[\nu]$ indicate stronger localization of the considered electronic state.

III. RESULTS AND DISCUSSION

A. Characterization of amorphous structures

We have analyzed the structural order in a-TiO_2 in terms of the reduced structure factor $F(q) = q[S(q) - 1]$ and its Fourier-transformed analogon, the reduced atomic pair-distribution function $G(r)$. From comparison to available experimental data[15] on structure factors and distribution functions, a mass density of 4.20 g/m^3, which is comparable to the density of the rutile phase, matches the reported experimental data[15] best and has, therefore, been chosen for further analysis. Choosing the same density as one of the crystal phases also allows the direct comparison of the electronic energy gap which commonly depends on the density. However, in consideration of the general dependence of electronic properties and optical transitions on the mass density, we will discuss the influence of density fluctuations exemplarily for the dielectric function at the end of this section.

In Fig. 2 the calculated reduced structure factor and reduced RDF [cf. Eq. (2)] for four amorphous unit cells are shown. As described in the methodology section, the position of the atoms in the unit cells have been optimized by MD approaches using DFTB and CPMD and structure relaxation via VASP.

The overall line shape of the structure factors is characterized by strong oscillations at smaller wave vectors with the most pronounced interference peak around a scattering vector magnitude of ~4 Å^{-1} and slightly decreasing amplitudes at higher magnitudes of the wave vector. The qualitative agreement in shape, peak positions, and amplitudes of the calculated and experimental data is particularly evident for the experimental x-ray diffraction (XRD) data on bulk TiO_2 powders. Moreover, the structure factor derived from electron diffraction measurements on radio frequency (RF) sputtered TiO_2 films deviates from the bulk powder result mainly in from of peak heights variations. Even the electron diffraction data on the sol-gel dip-coated TiO_2 films show a comprehensive agreement in peak positions, whereas the amplitudes for smaller magnitudes of the wave vector show substantial deviations. In general, experimentally observed differences in variously prepared amorphous TiO_2 samples may suggest that the short-range order is not uniquely determined by the particular chemical elements, but rather depends on the preparation route (cf. discussion by Petkov *et al.*[15]). However, the qualitative correspondences between experimental results and the simulated data indicate the unit cells' general ability to reproduce an adequate representation of the amorphous-phase structure in reciprocal and real space. From Fig. 2(a) also the DFTB approach's suitability to model a-TiO_2 is apparent. In general, the deviations between the variously simulated a-TiO_2 structures are less pronounced than differences between various experimental samples. Qualitatively similar conclusions can be drawn from an analysis of the RDF.

The RDFs, shown in Fig. 2(b), are characterized by a single sharp main peak slightly below 2 Å (~1.95 Å). This peak clearly arises from the first-neighbor, more precisely the first O ion shell, Ti-O correlations and agrees well with the Ti-O bond lengths between 1.8 Å and 2.1 Å found in the three main crystal phases of TiO_2. First-order O-O correlations are weakly indicated around 2.6 Å. The second main feature between 2.8 Å and 4.0 Å belongs to Ti-Ti pair correlations. The observed

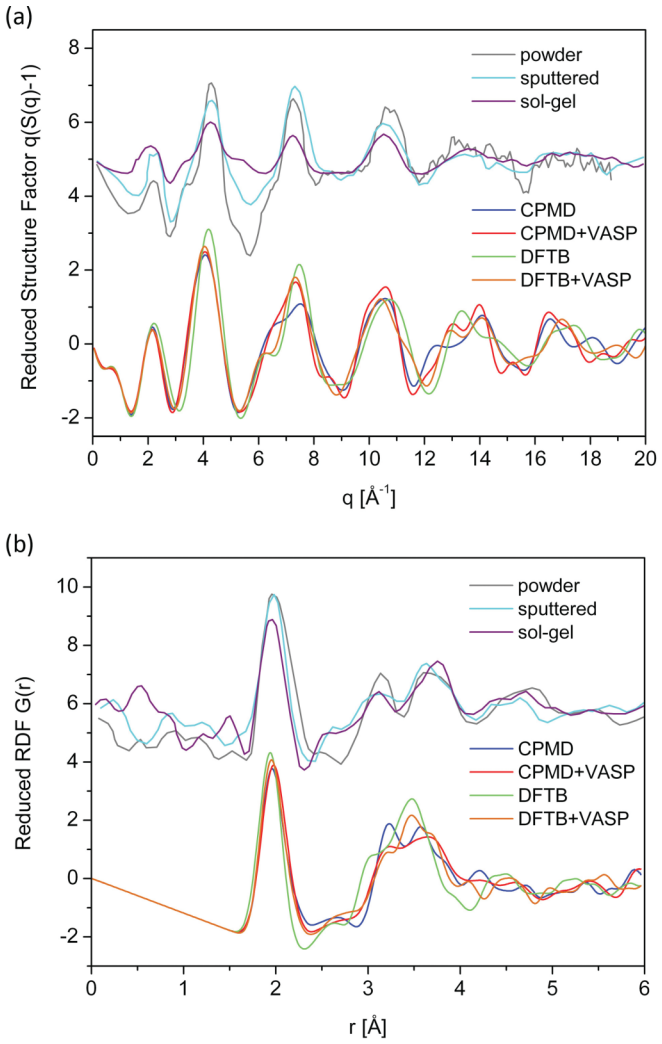

FIG. 2. (Color online) (a) Reduced static structure factors and (b) reduced atomic RDFs of DFTB, CPMD, and VASP optimized 4.20 g/m^3, 216-atom unit cells. Also displayed are the experimental results (extracted from Ref. 15) of diffraction experiments on sol-gel prepared and sputtered TiO_2 layers as well as TiO_2 powders.

two-peak characteristic reflects local symmetries characterized by edge-linked TiO_x building blocks with Ti-Ti distances around 3.2 Å and corner-linked TiO_x building blocks with Ti-Ti distances around 3.6 Å. The further curve progression shows exponentially decaying oscillations that arise from higher order pair correlations. The decay of long-range correlation further indicates the loss of long-range order in the amorphous material. However, the description of long-range contributions is limited by the confined unit cell volume. From comparison of the theoretical data curves with each other, quantitative differences in the first O coordination shell of Ti ions are small. Slightly more pronounced differences occur for Ti-Ti pair correlations. In general, a slight tendency of the main peaks towards lower distances is indicated in the DFTB data.

We have further analyzed the small differences between the MD results at room temperature (300 K) and the relaxed VASP structures, which formally represent the $T = 0$ K case, by a detailed investigation of the local atomic structure. In contrast to all non-high-pressure TiO_2 crystal phases, the local atomic environment in a-TiO_2 is not only characterized by sixfold coordinated Ti ions. In Fig. 1 we have used a polyhedra representation of TiO_x-polyhedron building blocks to identify differently coordinated Ti ions in the four investigated structure models of a-TiO_2. Based on the RDF's first main peaks, assigned to first-order Ti-O correlations, and the subsequent RDF's minima close to ∼2.3 Å, a 2.5 Å Ti-O bond-length cutoff was chosen for the polyhedron representation. The polyhedra representation immediately allows us to distinguish various types of short-range order.

In the case of the VASP relaxed CPMD configuration [see Fig. 1(b)], the amorphous unit cell contains 50% of TiO_6 building blocks and TiO_5 and TiO_7 units each with a fraction of 25%. Therefore, only half the Ti ions remain sixfold coordinated, while the other Ti ions gain or loose one O ion. As a consequence, the mean coordination number $Z_{Ti-O} = 6$ of Ti ions in (crystalline) octahedral-networks may be preserved in the disordered phase. This finding agrees with MD results published by Hoang[76] ($Z_{Ti-O} \approx 6$) and is in the error margin of $Z_{Ti-O} = 5.6 \pm 0.4$ reported by Petkov[15] for amorphous bulk powder samples.

The CPMD structure itself, which to some extent carries temperature influences on the atomic structure due to MD annealing to 300 K and a subsequent equilibration phase at 300 K, possesses a mean coordination number of Ti ions of $Z_{Ti-O} = 5.97$. The marginally smaller mean coordination is due to a 1.4% fraction of fourfold coordinated Ti ions. Nevertheless, despite the very similar coordination numbers, there are noticeable differences. TiO_6-polyhedron building blocks occur with an even higher fraction of 62%, while fivefold and sevenfold coordinated units occur with a ratio of 18.3% both.

As indicated by the RDF, the local atomic environment in the DFTB structure [see Fig. 1(a)] is slightly different from the structures generated by the other approaches. The DFTB structure exhibits a larger fraction of lower coordinated TiO_x-polyhedron building blocks. TiO_6, TiO_5, and tetrahedrally coordinated TiO_4 units occur with a ratio of 48% : 43% : 9%. As a consequence the mean coordination number is reduced to $Z_{Ti-O} = 5.4$ which agrees very well with the mean coordination number of $Z_{Ti-O} = 5.4 \pm 0.4$ found in Petkov's study for sputtered TiO_2 films[15] and is still in the error margin of the mean coordination number of the bulk powder samples. In the same study an even lower mean coordination number of $Z_{Ti-O} = 4.5 \pm 0.4$ was obtained for sol-gel prepared films. This low coordination reduces the amplitude of the reduced structure factor [cf. Fig 1(a)].

Finally the VASP relaxation of the DFTB geometry significantly increases the mean coordination number to $Z_{Ti-O} = 5.82$. In contrast to the other configurations, the remaining fraction of 2.7% fourfold coordinated Ti ions is mainly compensated by the occurrence of eightfold coordinated Ti ions. While TiO_5, TiO_6, and TiO_7 units occur with a ratio of 27.4% : 47.9% : 19.2%. We have summarized the TiO_x compositions and the mean coordination numbers of the four unit cells in Table I.

In summary, our simulation results indicate that short-range order in disordered material phases is nonunique. Nevertheless, the differences due to the use of different simulation methods are far smaller than the fluctuations

TABLE I. TiO_x polyhedron statistic (2.5 Å Ti-O bond-length cutoff) for the four 216-atom TiO_2 unit cells generated by CPMD, DFTB, and successive VASP relaxation.

Simulation approach	TiO_x building block fraction (%)					Mean coord. number
	TiO_4	TiO_5	TiO_6	TiO_7	TiO_8	
CPMD	1.4	18.3	62	18.3		5.96
CPMD + VASP		25	50	25		6.00
DFTB	9	43	48			5.40
DFTB + VASP	2.7	27.4	47.9	19.2	2.7	5.82

observed in the RDFs and structure factors of variously synthesized amorphous material samples. In detail, the atomic structure generated by DFTB MD is a good model for the sputtered TiO_2 films. On the other hand, the CPMD and VASP relaxed structures are closest to the bulk powder samples, characterized by mean coordination numbers close to the crystalline material. Furthermore, neither the DFTB nor the DFT structures seem to reproduce the very weak short-range order characteristics of the sol-gel prepared TiO_2 samples. This suggests a distinct local atomic environment in amorphous TiO_2 films prepared by the sol-gel technique and therefore a preparation specific short-range order in amorphous materials. Besides the significant disturbances in the local atomic structure by variations in the local and mean coordination numbers, also a notable fraction of the remaining TiO_6-polyhedron blocks in a-TiO_2 is significantly stronger distorted than in the brookite phase, which shows the lowest TiO_6 polyhedron symmetry among the main crystal phases. Hence, a central question in the further discussion will be how the physical properties in a-TiO_2 are modified as a consequence of these structural changes in local atomic order.

B. Electronic properties of amorphous TiO_2

After verifying the feasibility of describing the disordered material phase by our unit cells, we have investigated the local angular-momentum quantum number (l) decomposed density of states (DOS). According to Fig. 3 all four structure models are characterized by energy gaps that essentially do not contain defect states. Thereby, both VASP relaxed geometries show a comparable energy gap while the room-temperature structures show a significant energy gap reduction. Similar to the three crystalline main phases, the broad bands of occupied and unoccupied energy states show predominantly O_{2p}-like valence state and Ti_{3d}-like conduction state character. To some extent a hybridization between both types of electronic states is observed for occupied and unoccupied states. As a main characteristic of the crystalline material, the octahedral symmetry leads to a splitting of the unoccupied Ti_{3d} states into e_g and t_{2g} like subbands.[17,46,49,125,126] This distinct splitting is almost absent in the broad band of conduction states in a-TiO_2. Further analysis of the DOS, by decomposition of the l-decomposed DOS according to the magnetic quantum number m, also reveals a missing separation of the Ti_{3d}-like states into distinct energy-dependent d_{z^2}-, d_{xy}-, d_{yz}-, d_{xz}-, and $d_{x^2-z^2}$-like contributions. Again, this is in contrast to a well-defined separation in crystalline TiO_2.

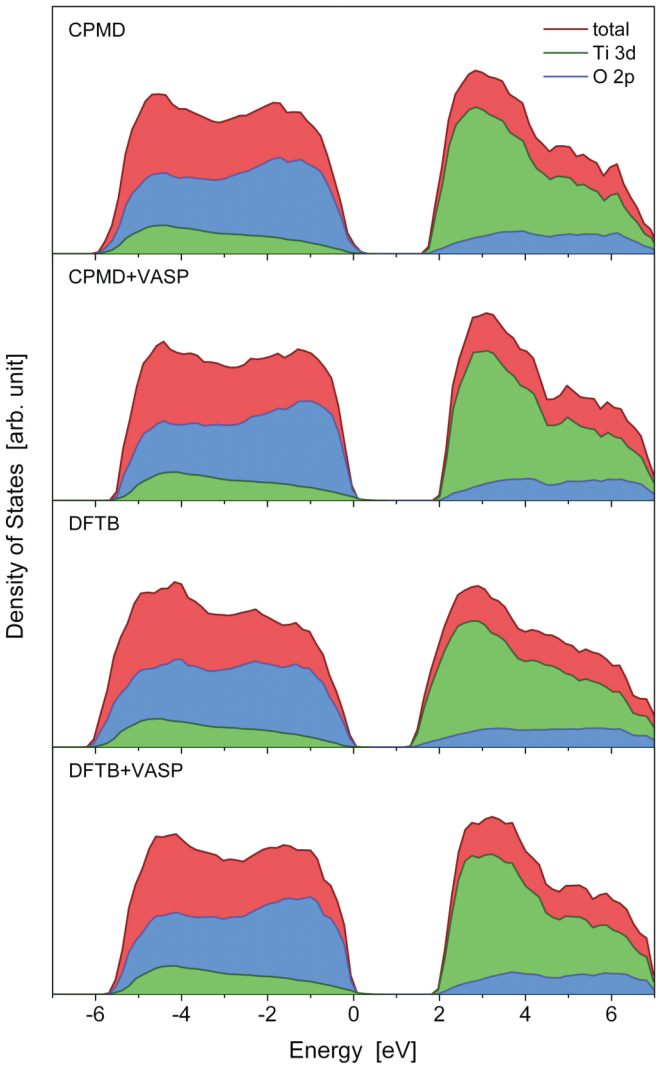

FIG. 3. (Color online) Total density of occupied and unoccupied states calculated from the DFT-PBE eigenvalues and local l-decomposed components for $3d$ states of Ti and $2p$ states of O.

From the representation of the DOS in Fig. 3, it is difficult to estimate the extent of valence and conduction band tails that are expected to form in a disordered material phase. A weak indication of band tails is given by the valence *band* edge in the DOS of the CPMD configuration. Also the significant energy gap reduction for the DFTB structure indicates the possible influence of band-tail states. In general, weakly pronounced band-tail features, depending on a small fraction of the electronic states of the complete system, are just weakly indicated in the electronic DOS due to its state counting nature and the numerically enforced broadening.

We used the VASP relaxed CPMD geometry to investigate the numerical description of the electronic structure of a-TiO_2 on different levels of theory in more detail. Figure 4 shows the eigenvalue spectrum obtained for Γ-point-only calculations using the PBE and HSE06 functionals. Due to the absence of periodicity and therefore a well-defined k vector, the electronic energy gap is simply given by the Kohn-Sham eigenvalue difference between the highest occupied and lowest unoccupied state. This definition is equivalent to the definition

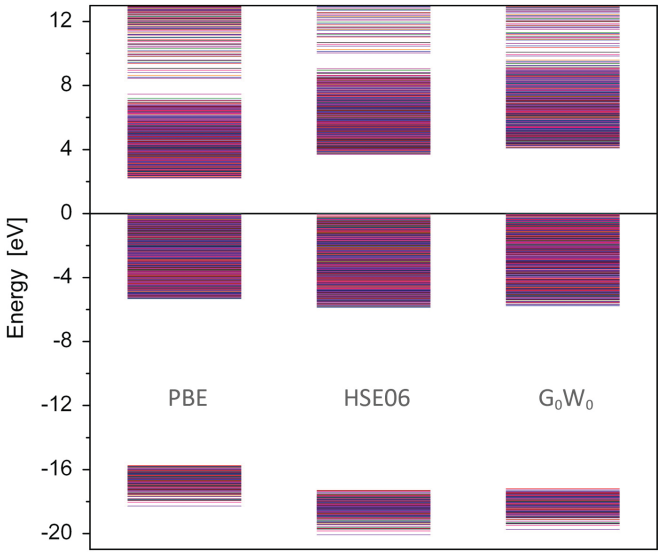

FIG. 4. (Color online) Kohn-Sham eigenvalues of the VASP relaxed CPMD structure calculated at the Γ point using the PBE and the HSE06 functional. Also shown are the QP energies obtained by G_0W_0 QP corrections on top of the PBE calculation. For details on the numerical convergence of the G_0W_0 results see discussion in the text.

of the HOMO-LUMO gap in molecular systems. The PBE energy gap of 2.21 eV is larger than the fundamental PBE gaps of the crystalline phases rutile (1.88 eV, direct), anatase (1.94 eV, indirect), and brookite (1.86 eV, direct). Using the HSE06 hybrid functional, the gap is widened to 3.69 eV which is close to the direct/indirect HSE06 anatase energy gap of 3.71 eV/3.60 eV. As demonstrated in our study on crystalline TiO_2,[17] the HSE06 eigenvalues represent a very accurate approximation of the QP energies, obtained from G_0W_0 calculations, as long as we consider energy states within ∼5 eV from the band edges. With this, the QP gap of the amorphous phase falls into the range of an anatase QP band gap of 3.7 eV to 3.9 eV estimated from the measured optical gap.

Also the G_0W_0 QP eigenvalue spectrum is presented in Fig. 4(c) and shows a large energy gap of 4.08 eV. However, this requires some comment concerning the numerical convergence of this value. Due to the large system size our G_0W_0 calculation was constrained to a set of minimal numerical parameters, mainly regarding the number of frequency grid points and the GW energy cutoff used to evaluate the response function. Aiming on a rough estimation of the associated error in the calculated energy gap, we applied a similar set of minimal parameters to the rutile bulk material. Similar to the enlarged energy gap of a-TiO_2, the obtained direct rutile band gap was 3.78 eV which is 0.46 eV larger than the converged result of 3.32 eV. Therefore, we expect that the G_0W_0 value of 4.08 eV overestimates the converged QP gap by ∼0.4 eV. Furthermore, the analysis of the rutile G_0W_0 QP gap convergence with the number of unoccupied bands (here: 2048, ∼28 per stoichiometric TiO_2 unit in a-TiO_2) further influences the result by at least 100–200 meV. The only approximation made in the HSE06 calculation was the reduction of the fast Fourier transformation grid in the exact exchange routines which significantly accelerates Hartree-Fock-type calculations. This typically adds an uncertainty not larger than a few hundred meV to the obtained band gaps. Compared to a calculation of the rutile phase using this limitation, the obtained HSE06 band gap is converged within ∼0.01 eV. The restriction to only the Γ point on the other hand does not influence the band gap notably. In fact the Γ point is even sufficient to obtain all characteristics of optical spectra.

From all these considerations, we expect the HSE06 energy gap of 3.69 eV to be a very reliable value for the QP gap of a-TiO_2.

Reported experimental energy gap data on variously prepared a-TiO_2 thin films cover an energy range from 3.2 eV to 3.7 eV.[24,26–33,35,36,127] All these results were obtained from UV-VIS spectroscopy followed by direct or indirect Tauc analysis/plots[128–130] to extract the optical gap. This means $(\alpha E)^{1/2}$ or $(\alpha E)^2$, with α being the absorption coefficient, is plotted versus the photon energy and the linear part of the curves is extrapolated towards the energy scale to define the optical gap. Besides UV-VIS spectroscopy data, we are not aware of any photoemission-spectroscopy data on a-TiO_2 that allow a direct verification of the calculated QP result. Therefore an experimental QP gap could only be estimated to be larger than the measured optical gap. A more accurate data examination shows a cumulatively reported optical gap between 3.2–3.5 eV,[26,29,31,32,36] obtained from indirect Tauc analysis $(\alpha E)^{1/2}$, and an energy gap >3.6 eV,[33] determined by direct Tauc analysis $(\alpha E)^2$ of the Kubelka-Munk function[131,132] that is proportional to the absorption coefficient.

Besides the exact energy gap value, general tendencies within the existing TiO_2 modifications are of interest in order to identify materials best suited for an intended usage and to understand underlying physical principles in general. While there is clear experimental evidence for an amorphous phase energy gap that is larger than the band gap in TiO_2 rutile, the relation $E_{\mathrm{gap}}^{\mathrm{am}} \gtrless E_{\mathrm{gap}}^{\mathrm{an}}$ between amorphous and anatase TiO_2 is unclear. Even the relation $E_{\mathrm{gap}}^{\mathrm{an}} \gtrless E_{\mathrm{gap}}^{\mathrm{br}}$ between the band gaps of crystalline anatase and brookite seems not completely unambiguously decided by experimental literature data. Since experimental data on TiO_2 brookite is limited and theoretical calculations[17] favor $E_{\mathrm{gap}}^{\mathrm{an}} > E_{\mathrm{gap}}^{\mathrm{br}}$, we will focus on the energy gaps of anatase and a-TiO_2. On the one hand, Amor *et al.*[24] demonstrated a sharp rise of the energy gap from 3.46 eV to 3.54 eV at the anatase crystallization temperature (350 °C) during annealing of a-TiO_2 films. Mardare *et al.*[35] estimated the optical gap of a-TiO_2 films to 3.25 eV and to 3.4 eV in crystalline anatase films. Also, a large band gap value of 3.8 eV for direct optical absorption in anatase TiO_2 films was obtained by Wang *et al.*[34] In addition Gofuku *et al.*[29] obtained identical energy gaps (3.4 eV) for both amorphous and anatase films. On the other hand, direct optical gaps of ∼3.4 eV for anatase and 3.66 eV for amorphous TiO_2 have been published by Luca *et al.*[33] Mardare *et al.*[27] observed an energy gap decreasing from 3.37 eV to 3.01 eV with increasing annealing temperature causing anatase formation. However, the behavior in the last study seems to be caused by the notable and, at higher temperature, even major coexisting fraction of the rutile TiO_2 phase. Within our theoretical description the

HSE06 calculations had shown almost identical energy gaps of 3.69 eV and 3.71 eV for a-TiO_2 and anatase. The assumption of similar electronic energy gaps in anatase and amorphous TiO_2 is further supported by results for mixed anatase-amorphous phases. DeLoach *et al.*[127] reported an indirect band gap of 3.41 eV for thin TiO_2 films build up by coexisting anatase and amorphous phases and a small volume fraction (0.02–0.017) of rutile.

We conclude that the pure stoichiometric amorphous phase of TiO_2, with an atomic density close to the rutile phase, shows a QP gap $\gtrsim$3.7 eV that is larger than the experimental and theoretical values reported for rutile and brookite, and that is comparable to the theoretically determined anatase QP band gap, as well as to the reported direct optical gaps of anatase thin films. So far we have restricted the discussion to the HOMO-LUMO-type energy gap, which, as we will see in the following section, was the main reason for choosing one of the VASP relaxed configurations due to the reduced influence of band-tail state localization.

C. Localization of band-tail states

In order to characterize the band-tail states, that were only weakly indicated in the electronic densities of states, we have calculated the information entropy based quantities $W^{-1}(\nu)$ and $R^{-1}(\nu)$ [cf. Eqs. (13), (14), Sec. II D] for the four structure models investigated here. Both representations give qualitatively similar information on the degree of electronic localization. Due to the difficulty to clearly distinguish between the localized and extended states, the determination of the mobility gap remains uncertain to some extent. Nevertheless, both the $W^{-1}(\nu)$ and $R^{-1}(\nu)$ representation allow a qualitative analysis of electronic state localization and the estimation of the mobility edge within a few tenths of an eV. In Fig. 5, the estimated separation between localized and extended states is indicated by vertical dashed lines, whose positions were chosen from the distinct quantitative differences in $W^{-1}(\nu)$ and $R^{-1}(\nu)$ values for the two VASP relaxed configurations. As a general limitation we have to keep in mind that the sizes of our unit cells represent a severe limitation to the accurate

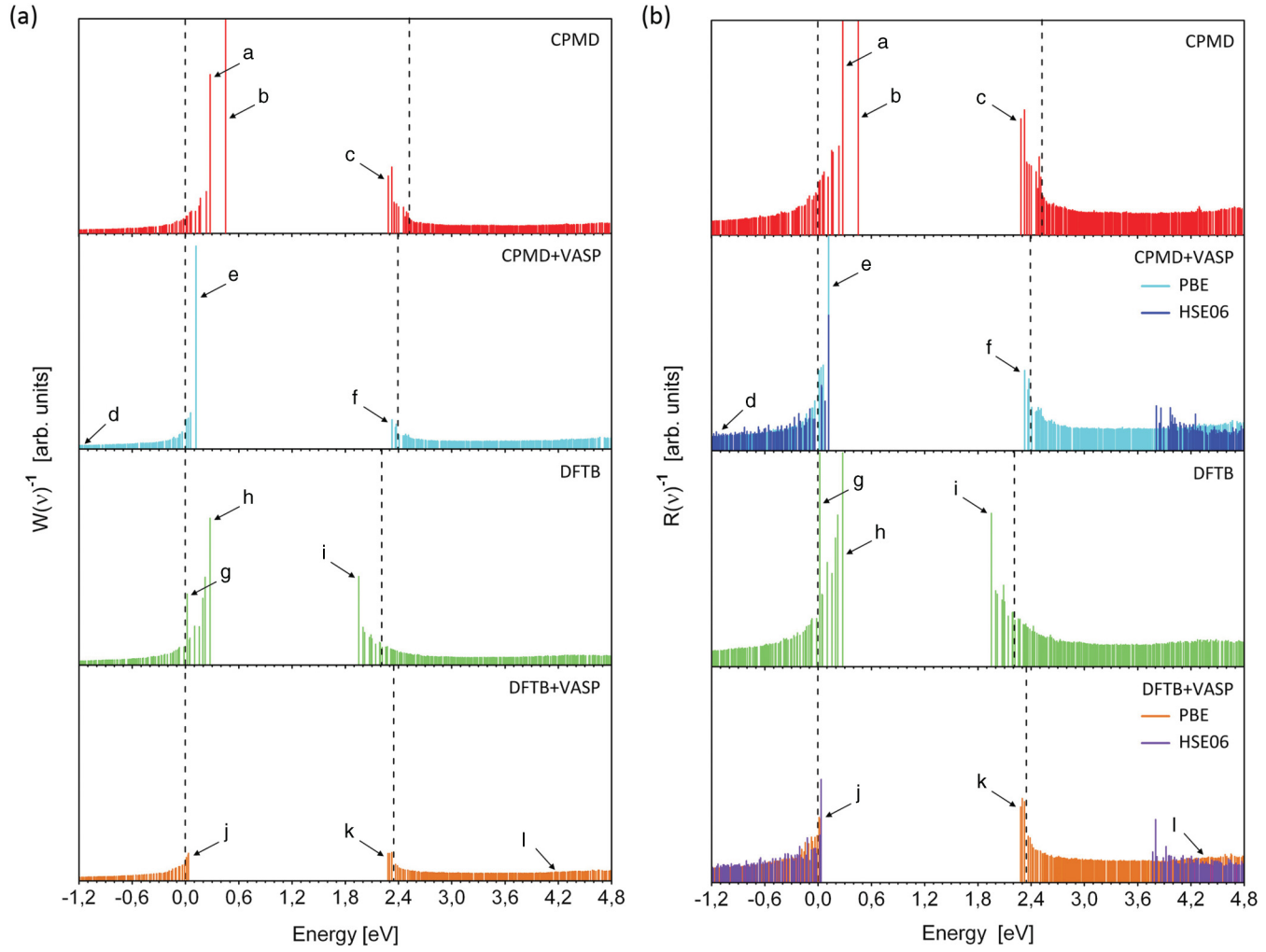

FIG. 5. (Color online) Information entropy based measures of state localization $W^{-1}(\nu)$ and $R^{-1}(\nu)$ for the CPMD MD and DFTB MD generated as well as VASP relaxed models of 4.20 g/cm^3 a-TiO_2 (cf. Fig. 1). Based on the definitions in Sec. II D, a higher value corresponds to stronger localization for both quantities. For the two VASP optimized structures, the IPRs based on the HSE06 electron densities have been included. The DFT-PBE electron densities for marked electronic states are visualized in Fig. 6. Also indicated are the estimated positions of the mobility edges that separate the strongly localized states from the delocalized Bloch-type states. The estimated position of the valence states mobility edge has been chosen as the zero point of the energy scale (x axis).

modeling of localized states and the transition to extended states in an amorphous material phase.

In Fig. 5, we clearly observe extended valence and conduction band tails for the two room-temperature structures generated by CPMD and DFTB MD. These band tails are responsible for the smaller HOMO-LUMO-type energy gaps at room temperature structures. We find the weakest formation of band-tail states for the VASP relaxed DFTB geometry. However, the VASP relaxation of the CDMD generated structure shows equally weak pronounced band-edge tails with exception of the highest distinctly localized valence state. These observations, in general, demonstrate a significant influence of temperature-induced disorder on the localization of electronic states. Interestingly, the formation of band-tail states does not directly seem to be correlated to the mean coordination number. While the mean coordination number decreases significantly for the DFTB geometry, no significant difference to the crystalline mean coordination was found in the CPMD geometry as already discussed above.

In detail the estimated mobility gaps of the VASP relaxed CPMD and DFTB structures are 2.39 eV and 2.35 eV which is only slightly larger than the energy differences of 2.21 eV and 2.25 eV of the lowest occupied and the highest unoccupied state, respectively the HOMO-LUMO-type gap. Compared to the DFT-PBE band gaps of the crystalline TiO_2 phases (rutile: 1.88 eV, anatase: 1.94 eV, and brookite: 1.83 eV), the gap energies increase about $\sim$0.4 eV due to structural disorder. The mobility gaps of the two room-temperature MD configurations show no clear tendency in the development of the mobility edge due to temperature-induced disorder. On the one hand, the band-tail states' adjusted gap of the CPMD structure increases to 2.52 eV. On the other hand, the same quantity is reduced to 2.21 eV in the case of the DFTB structure.

Figure 5 also displays the IPR based on the electron densities from HSE06 calculations for the two VASP optimized structure models. In both cases the HSE06 data show quite similar localization characteristics. Similar to the PBE data, the valance tail shows a slightly more distinct localization of band-tail states. Based on the HSE06 calculation, we obtain an estimated mobility gap of $\sim$3.8 eV for both a-TiO_2 structure models. Similar to the PBE data these gaps are only slightly ($\sim$0.1 eV) larger than the HOMO-LUMO-type energy gaps of 3.69 eV and 3.73 eV for the CPMD + VASP and the DFTB + VASP structures.

In order to classify the nature of the localized band-tail states, we have selected characteristic examples of localized electronic states and visualized the electronic charge-density distributions in Fig. 6. Despite their spatial localization, we find that all band-tail states conserve the O_{2p}-like valence state and the Ti_{3d}-like conduction state character. The electronic states labeled by a and b for the CPMD structure as well as e and h for the CPMD + VASP and DFTB structures represent the strongest localized states found in our models. The nature of these localized valence states can be assigned to two types of lattice sites. On the one hand, we find *p*-type charge density contributions from threefold coordinated O ions that are slightly displaced from the plane of the three Ti ions in Ti_3O units. On the other hand, we find significant contributions from under-coordinated O ions, bound to just two Ti ions. Also the less confined electronic state visualized in Fig. 6(j), that forms the highest valence state in the VASP relaxed DFTB configuration, belongs to this type of localized states. The localized conduction band-tail states, in all configurations, arise from charge densities located at over-coordinated Ti ions in TiO_7 building blocks as well as contribution from formally sixfold coordinated TiO_6 and, to a minor extent, from under-coordinated TiO_5 building blocks.

We have also included examples of completely delocalized Bloch-type states. Figure 6(d) exemplarily represents states out of the continuum of delocalized O_{2p}-like states in a-TiO_2. The charge density distribution in Fig. 6(l) belongs to the class of delocalized Ti_{3d}-like states in a-TiO_2. Similar to crystalline TiO_2 the optical characteristics of a-TiO_2 are thus expected to be significantly characterized by optical transitions between these two continua of Bloch-type states.

A more detailed representation of the dependence of the local coordination number and the character of associated electronic states is given in Fig. 7. Here, the local/site-decomposed densities of states are displayed for the various coordinations of O and Ti ions found in the CPMD + VASP configuration [cf. Fig. 1(b)]. In agreement with the charge densities of the different localized valence-tail states pictured in Fig. 6, the topmost valence states show a characteristic predominance of under-coordinated oxygen ions in Ti_2O filaments. Energetically slightly lower lying states show the common threefold coordination of the most common crystalline phases (cf. Ref. 17). As mentioned above, the corresponding Ti_3O units show structural distortions from the planar-trigonal crystal-type building blocks. Hence, the valence band tail arises primarily from localized states due to variations of the local oxygen coordination number and additional contributions from state localization due to structural disorder in deformed Ti_3O building blocks. The DOS contributions of over-coordinated, distorted-tetrahedron-type Ti_4O building blocks show a clear separation from the contributions of lower coordinated O ions and a dominant contribution at the bottom of the first valence *band*. The DOS differences in the lower half of Fig. 7(a) indicate that the amounts of lower coordinated and higher coordinated DOS contributions show an approximately antiproportional distribution over the whole energy range.

While the observable energetic separation of differently coordinated ions in the local DOS gives rise to the slightly more pronounced valence tails of a-TiO_2 indicated by the IPR in Fig. 5, the conduction band edge shows a stronger superposition of states originating from differently coordinated ions. Over-coordinated TiO_7, normal-coordinated TiO_6, and under-coordinated TiO_5 building-block states occur directly at the conduction band-tail edge. In general, a slight preference for higher coordination is still notable at the bottom of the conduction *band*, whereas, at higher energies, the superposition of DOS contributions from different coordinations is less structured.

Bridging the gap to language and concepts bound to a common view of deviations from a normal crystal-type atomic coordination as defects, we may also recover the characteristics of donor- and acceptor-like states. The unpaired electrons of the under-coordinated O ions generate localized acceptor-like dangling bond states at the valance band-tail edge. The local over-coordination of Ti ions on the other hand results in the presence of localized donor-like electronic states at

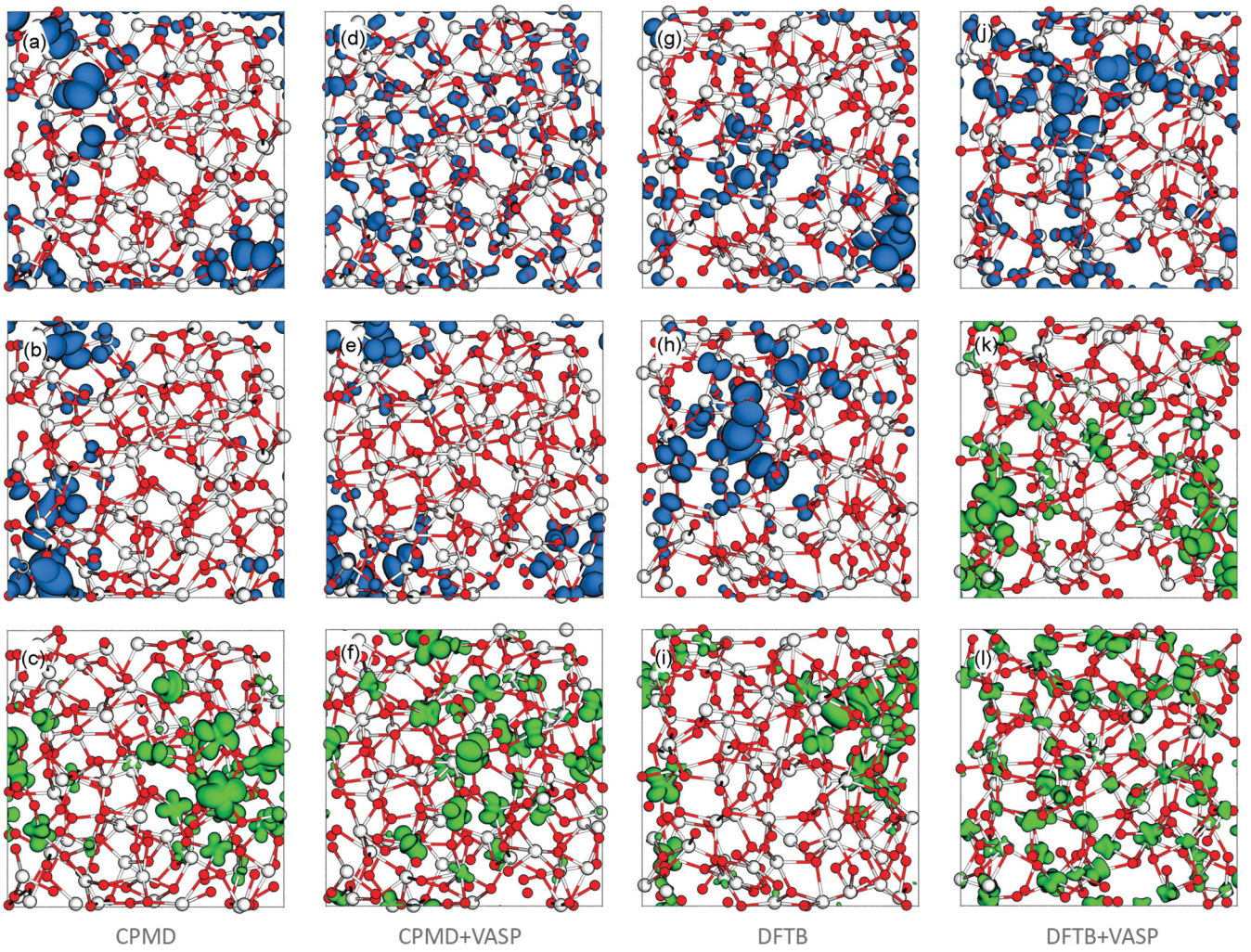

FIG. 6. (Color online) Isosurfaces of various electronic states in a-TiO_2. The states are labeled corresponding to the energy levels in Fig. 5. The states represent different degrees of localization for occupied and unoccupied states. The subfigures d and l are examples for completely delocalized Bloch-type states.

the conduction band-tail edge. Similar to the well-defined separation of bonding and antibonding states discussed above and the resulting crystal-like electronic structure, the formation of crystal-type defect states due to over- and under-coordinated ions demonstrates the strong influence of short-range order on the formation of the electronic structure in disordered semiconductors.

D. Optical properties of amorphous TiO_2

To obtain more insight into the optical characteristics of a-TiO_2 we investigated the dielectric function and related frequency-dependent optical constants of our structure models over an extended energy range. In Fig. 8, the real and imaginary parts of the calculated IPA dielectric functions are shown for all four unit cells. As already indicated by the structural characteristics in Sec. III A and the electronic properties described in Sec. III B, the CPMD, CPMD + VASP, and DFTB + VASP configurations show almost identical dielectric properties. Also the DFTB MD generated structure shows very similar spectral features with some variations in peak heights. Thus, in the following discussion, we will focus on the VASP relaxed CPMD configuration and compare the results obtained for the DFTB structure at the end of this section. For simplicity we will refer to the CPMD + VASP structure just as the VASP configuration. Considered together, these two structures allow us to estimate the variations in the optical properties originating, on the one hand, from the room-temperature influences on electronic structure, and on the other hand from different types of local symmetries, generated by various numerical approaches.

The optical frequency-dependent constants of a-TiO_2, defined through Eqs. (3)–(7), are displayed in Fig. 9. More precisely the plotted curves correspond to the isotropic optical functions obtained by averaging the nonvanishing components of the dielectric tensor [i.e., $(\varepsilon_{xx} + \varepsilon_{yy} + \varepsilon_{zz})/3$]. Without these averaging procedures, the obtained dielectric functions still show some weak anisotropies due to the limited super cell size while the qualitative distribution of oscillator strength is identical. Instead of using the insufficiently converged G_0W_0 results to derive QP shifts, we applied the scissors-shift approximation to shift the unoccupied DFT-PBE Kohn-Sham

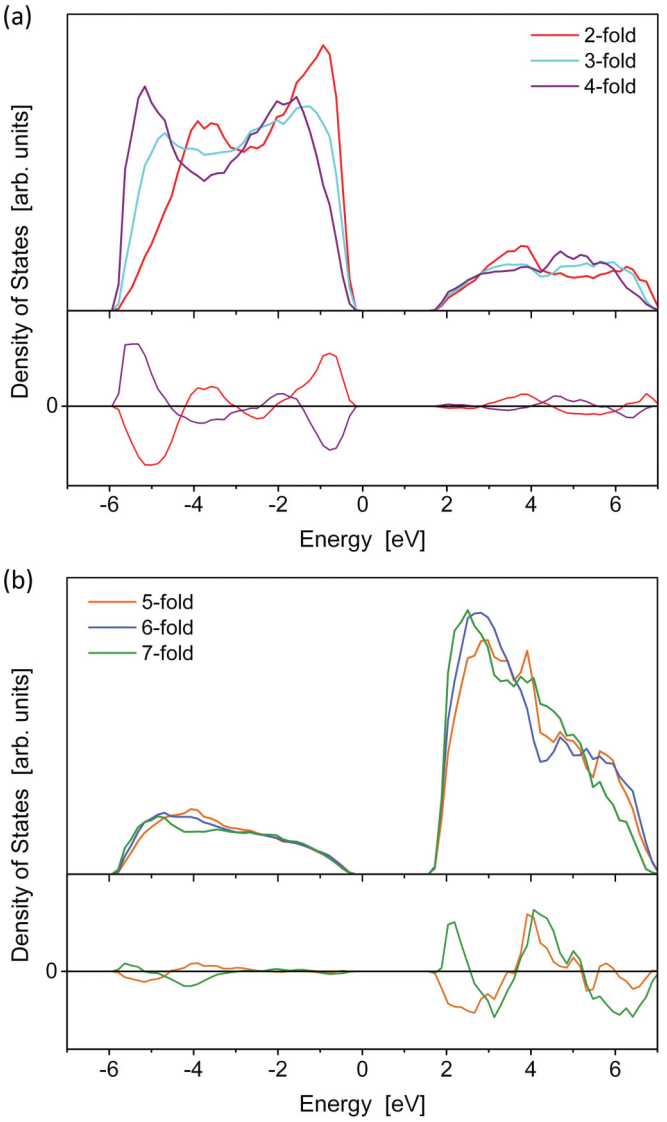

FIG. 7. (Color online) Local densities of states for the various coordination numbers occurring in the CPMD + VASP model. The total site-projected densities of states have been averaged over all O ions (a) and Ti ions (b) showing the particular coordination. The lower graphs show the differences between the normal coordinated ions (threefold in the case of O ions and sixfold for Ti ions) and the over- and under-coordinated ions.

states in energy while keeping the PBE wave functions to calculate matrix elements. Motivated by scissors shifts of 1.2 eV, 1.3 eV, and 1.3 eV for the crystalline phases rutile, anatase, and brookite [chosen to match direct optical band gaps of rutile and anatase (cf. Ref. 17)], we applied a scissors shift of 1.3 eV for our a-TiO_2 models. In contrast to the DFT-PBE eigenvalue spectrum in Fig. 4, the optical spectra were calculated using a regular $3 \times 3 \times 3$ k-point mesh. However, the restriction to one k-point only results in oscillations of the oscillator strength in the dielectric function's main peaks that are small if compared to the results obtained by the coarser k-point grid.

Figure 9(a) shows the real and imaginary parts of the dielectric function calculated using 1920 electronic bands and

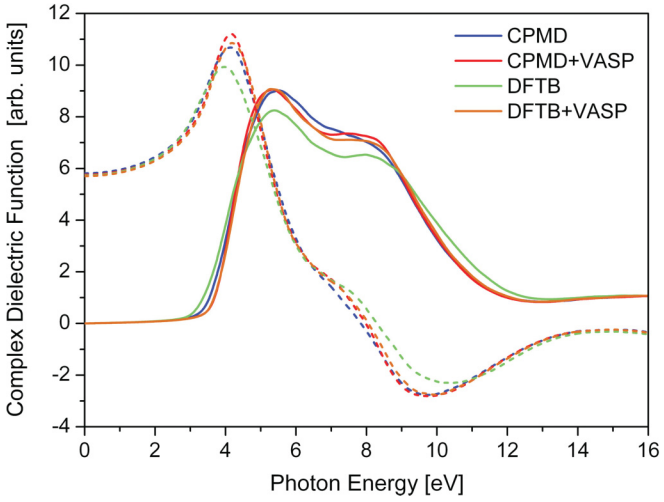

FIG. 8. (Color online) Real (dashed line) and imaginary (solid lines) parts of the isotropic complex dielectric functions $\varepsilon(\omega)$ of the four a-TiO_2 models (cf. Fig. 1).

a Γ-centered $3 \times 3 \times 3$ k-point mesh. By extrapolating the linear low-energy flank of the imaginary part of the dielectric function towards the energy axis, the absorption onset around ∼3.65 eV is found to be close to the minimal estimated value for the QP gap. This tendency is quite similar to the difference in QP band gaps and extrapolated optical band gaps of the crystalline phases obtained from solving the BSE for Coulomb correlated QP.[17]

Compared to very recent data for ion-beam sputtered films [see red dotted curves in Fig. 9(a)] that indicate the absorption onset around 3.6 eV, our calculated dielectric function is found to be in good agreement with the experiment. Also, the real part of the dielectric function demonstrates a fairly reasonable agreement between theory and experiment on the dielectric constants in the visible range of the spectrum. Comparing the dielectric constants at 2 eV (i.e., a wavelength of 620 nm), we find an agreement between the experimental value of $\varepsilon(620\ \text{nm}) = 5.93$ and the theoretical result $\varepsilon(620\ \text{nm}) = 6.37$ within ∼7%. Unfortunately the measured dielectric function data are limited to a small energy region around the absorption onset, and we cannot compare spectral features at higher energies. An extended spectroscopic ellipsometry data set for the complex refractive index of electron-beam evaporation prepared TiO_2 thin films is found in the literature,[30] spanning an energy interval from 1.5 eV to 5.5 eV. These results are included in Fig. 9(b). The experimentally observed peak at 4 eV in the real part of the complex refractive index $\tilde{n}$, respectively the refractive index n, is qualitatively resolved in our data, while the peak height is noticeably underestimated and the peak position is slightly overestimated by ∼0.2 eV. However, the refractive index in the visible range around 2 eV [$n(620\ \text{nm}) = 2.52$] agrees perfectly with the experimentally derived data. Additionally we have summarized the further available data on the refractive index $n(\lambda)$ and the extinction coefficient $\kappa(\lambda)$ (mainly given for 500–600 nm green light) in Table II.

These collected experimental dielectric constants give further evidence for a reasonable description of optical constants by our data, even though the calculated values tend to

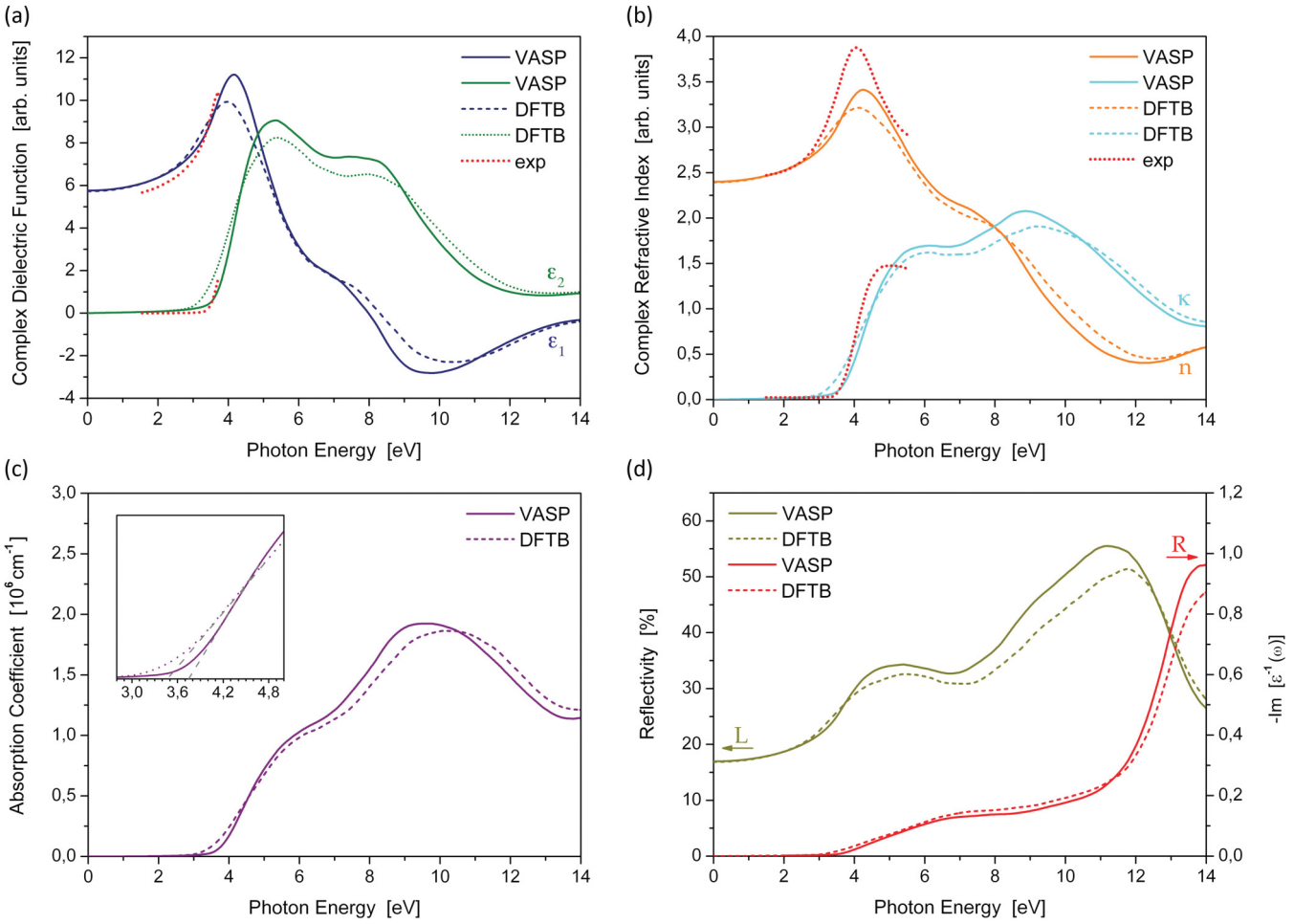

FIG. 9. (Color online) (a) Real part $\varepsilon_1(\omega)$ and imaginary part $\varepsilon_2(\omega)$ of the complex dielectric function $\varepsilon(\omega) = \varepsilon_1(\omega) + i\varepsilon_2(\omega)$, (b) real part $n(\omega)$ and imaginary part $\kappa(\omega)$ of the complex refractive index $\tilde{n} = n + i\kappa$, (c) absorption coefficient $\alpha(\omega)$, and (d) reflectivity $R(\omega)$ (left axis) and energy loss spectrum $R(\omega)$ (right axis). The optical spectra are calculated from the DFT-PBE eigenvalues (CPMD + VASP or DFTB structure, 1920 electronic bands, $3 \times 3 \times 3$ k points) applying a scissors shift of 1.3 eV to the unoccupied states. For comparison, experimental data for the dielectric function from Ref. 133 and refractive data from Ref. 30 have been included.

overestimate the measured ones up to 20%. Generally, one should keep in mind that the reported data are significantly influenced by temperature[135] and density fluctuations of the films.[134] A comparison of the calculated imaginary part of the complex refractive index, i.e., the extinction coefficient κ, to plotted experimental result in Fig. 9(b) shows a deviation in peak height and position but still comparable curve characteristics. The calculated extinction coefficients in the visible wavelength regime (see Table II) are significantly overestimated. However, the description of such small absolute values is beyond the accuracy of the applied theoretical framework. Errors of this size are already caused by the choice of the broadening parameter for evaluating the dielectric function.

In Fig. 9(c) the absorption coefficient for the amorphous material is given. The inset gives a detailed view of the absorption coefficient around the adsorption onset. From the linear rise of the absorption coefficient and linear extrapolation to the energy axis, the energy gap has been estimated to 3.74 eV, which is in the region of the (estimated) QP gap. At this point an additional comment on the determination of energy gaps from experimental data seems appropriate. Basically, all the discussed experimental data on TiO_2 thin

TABLE II. Experimentally determined refractive indices $n(\lambda)$ and extinction coefficients $\kappa(\lambda)$ in the visible range measured for variously prepared (predominantly) amorphous TiO_2 thin films. To preserve clearness, only the values for experimental conditions closest to the theoretical calculation (0 K and 4.20 g/cm^3) are included.

Wavelength (nm)	n	κ	Film preparation	Ref.
500	2.51	3×10^{-3}	ion-beam evaporation	134
550	2.51		bias arc ion plating	36
550	2.40		DC sputtering	25
550	2.57	$\sim 10^{-4}$	vacuum arc deposition	32
552	2.21	0.8×10^{-3}	DC sputtering	27
600	2.24	2.6×10^{-3}	magnetron sputtering	135
600	2.12	1.8×10^{-3}	magnetron sputtering	26
500	2.61	23×10^{-3}	this work	
550	2.56	19×10^{-3}	this work	
600	2.53	16×10^{-3}	this work	

films (crystalline, nano/micro-crystalline, or amorphous) rely on the, strictly speaking empirical, fitting of an exponential law to the measured absorption data. Thereby, the actual value of the exponent is related to the assumption of direct or indirect optical transitions. To demonstrate the ambiguity of the various optical-gap extrapolation methods, we obtain an energy gap of 3.34 eV from analyzing $(\alpha h\nu)^{1/2}$, 4.5 eV from $(\alpha h\nu)^2$, and 3.74 eV in the case of analyzing α itself. Moreover, the differentiation into "direct" and "indirect" transitions or the denotation "band" gaps is misleading in the case of an amorphous phase, since these are concepts of crystalline materials with a well-defined k vector and cannot be applied to amorphous solids. However, the 3.34 eV gap energy, obtained from analyzing $(\alpha h\nu)^{1/2}$ for our calculated absorption coefficient, agrees with the reported thin film values of 3.2–3.5 eV obtained from indirect Tauc analysis. In this way our results support the empirically motivated fitting procedure to derive energy gaps from amorphous samples by using the extrapolation of the linear progression in $(\alpha h\nu)^{1/2}$ to define the optical band gap. For the sake of completeness, the energy-dependent reflectivity and the (low) energy loss spectrum have been calculated from the dielectric function; see Fig. 9(d).

Throughout all optical spectra, the frequency-dependent optical constants calculated for the 300 K DFTB-MD geometry show qualitatively identical spectral features. However, the slightly different type of short-range order, which is for example indicated by the lower mean coordination number of Ti ions, seems to result in some spectral weight relocation away from the center of the main peaks in the imaginary part of dielectric function towards the low- and high-frequency flanks. This also reflects the reduced energy gap obtained for the DFTB geometry. The differences in the imaginary part of the dielectric function also affect the peak heights in the real part. Nevertheless, the spectrum in the visible range coincides with the VASP structure data curve in that region. From extrapolating the linear parts in the imaginary part of the dielectric function and the absorption coefficient, energy gaps of ∼3.35 eV and ∼3.49 eV are obtained. These values are 0.25 eV and 0.3 eV below the corresponding quantity calculated from the VASP optimized structure.

Altogether, the structure provided by the numerical efficient DFTB-MD simulation allows a cost-efficient generation of amorphous structures with optical properties that are very close to the properties of CPMD-MD results. After additional (zero temperature) DFT structure relaxations of the DFTB-MD and CPMD-MD configurations, no significant differences in the dielectric functions (cf. Fig. 8) remain.

E. Many-body contributions to the optical response of amorphous TiO_2

The preceding discussion of optical properties was strictly based on a pure DFT-PBE single-particle picture for the dielectric function (i.e., IPA). In order to estimate the influence of many-particle interactions on the optical response of the many-electron system, we have treated one- and two-particle excitation within the framework of many-body perturbation theory in the commonly applied two-step procedure.

In a first step we consider QP self-energy corrections to the eigenvalue spectrum by the first-order perturbative G_0W_0 approach. The resulting QP energies determine the dielectric function in independent QP approximation (IQPA). Compared to the IPA dielectric function (without taking into account a scissor shift correction), the IQPA dielectric function (see Fig. 10) shows a strong blueshift of the absorption edge of ∼1.85 eV but almost identical spectral features. As discussed in the context of electronic energy gaps, this strong blueshift might suffer from an overestimation of QP shifts by ∼0.4 eV that is owned to the indispensable reduction of numerical parameters in our G_0W_0 calculation. As shown elsewhere (see Ref. 17), the use of the HSE06 hybrid functional allows an accurate approximation of TiO_2 QP properties. Thus, we expect the the HSE06 energy shifts/the HSE06-IPA dielectric function to be more reliable. In analogy to the energy gap, the blueshift (∼1.5 eV) of the absorption edge is less pronounced by using the hybrid functional data.

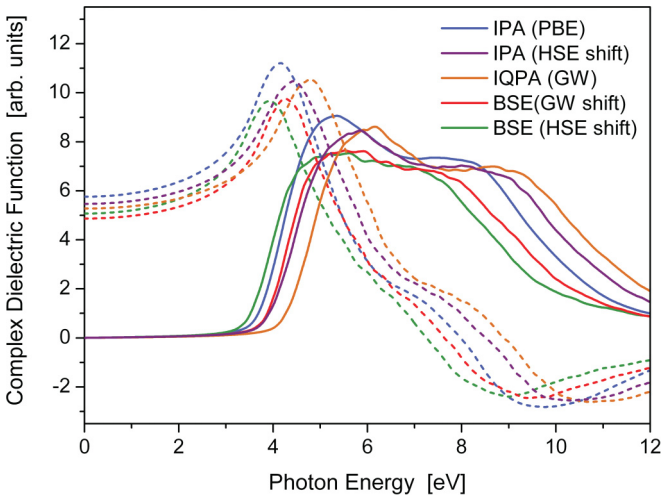

FIG. 10. (Color online) Real (dashed line) and imaginary (solid lines) parts of the isotropic complex dielectric function $\varepsilon(\omega)$ calculated for the CPMD + VASP structure model on different levels of theory.

The second step of many-particle effect-inclusion accounts for two-particle electron-hole pair excitations (i.e., excitonic effects) and necessitates the computational demanding solution of a Bethe-Salpeter equation for Coulomb correlated (quasi)particles. For the most common crystalline phases distinct modifications of the optical response have been observed[17,59,60,62] by inclusion of the two-particle excitations. On the one hand the absorption onset is redshifted compared to the IQPA data. On the other hand electron-hole pair interactions add and modify spectral features in the optical response functions. In particular, characteristic excitonic feature are found in the dielectric function of rutile and anatase close to the adsorption onset. For the symmetry-reduced TiO_2 brookite phase these excitonic features are found to be less pronounced.[17] Obviously these trends hold for a-TiO_2. The BSE dielectric functions show an absorption edge redshift of ∼0.5 eV compared to the IQPA-G_0W_0 respectively the IPA-HSE06 dielectric function.

Apart from the redshift, no distinct excitonic modifications of the BSE dielectric function are found. In summary, the main effect of many-body contributions to the linear optical response is a pronounced energy shift while the spectral

weight distribution is widely preserved. All together, these observations provide a sufficient justification for the computationally efficient use of the well-converged IPA dielectric function in combination with a simple scissors shift approximation. Some of the differences between the scissor shifted IPA and the BSE dielectric function may also be related to the numerical setup used to solve the BSE. Especially, the reduction of the energy cutoff for pairs of Kohn-Sham eigenvalues that enter the constructing of the electron-hole pair Hamiltonian, the restriction to only the Γ point, and the energy cutoff for evaluating of the Kohn-Sham-Bloch matrix elements add some uncertainty to the BSE dielectric function.

F. Order and disorder in optical spectra

In this subsection we will address the question of how the optical properties of the crystal are modified by its loss of long-range order in the context of a further analysis of the complex dielectric function. In order to single out the differences between the amorphous and crystalline phases, the isotropic real and imaginary parts of the IPA dielectric functions of rutile, anatase, and brookite are plotted in Fig. 11 alongside the result for the amorphous material (CPMD + VASP structure). In contrast to the most common crystalline phases, the imaginary part of the dielectric function of a-TiO_2 indicates stronger absorption in the energy range between 5 eV to 8 eV by an enhanced oscillator strength in this energy region. Nevertheless, the two main-peak characteristic observed in the spectra of crystalline TiO_2 remains identifiable. Similar to anatase, the center of the first main peak is slightly shifted to higher energies (∼5.3 eV) compared to rutile.

The comparison of the isotropic dielectric functions again prove the common optical characteristics of rutile, anatase, and brookite. However, despite the suggested close relation of a-TiO_2 to brookite or anatase, pronounced differences are obvious. Even the equally weighted average over the three crystalline main phases does not show any more resemblance to a-TiO_2. The reason for the differences can be traced to the differences in the local atomic structure already emphasized in the discussion of structural properties in Sec. III A. For the crystalline phases rutile and anatase the existence of the two peaks has been assigned to the crystal-field spitting[17,48,49,125,126,136] of the unoccupied broad Ti_{3d} energy band into e_g and t_{2g} like subbands. This splitting is directly connected to the local octahedral coordination of a Ti ion by six O ions, which even holds for the stronger distorted octahedra in the symmetry-reduced brookite phase. Since the octahedral-like local symmetry is partially lifted in the amorphous phase due to strong distortion in the TiO_6 building blocks and the formation of TiO_x units with $x = 4, 5, 7, 8$, this characterization cannot be applied to the entire amorphous material complex. Due to the missing distinct separation of Ti $3d$ states into e_g and t_{2g} like states, optical excitations take place between two broad energy continua of electronic states whose types are exemplarily visualized in Fig. 6(d) and Fig. 6(l). These are on the one hand the occupied $2p$-like states of oxygen, covering the energy range from −5.3 eV to 0 eV, and on the other hand the unoccupied $3d$-like states in the energy region from 3.5 eV to 8.8 eV. Here, the energy of the highest occupied Kohn-Sham state has been chosen as the zero point of the energy scale and, in contrast to the l-DOS reported in Fig. 3, a scissors shift of 1.3 eV has been taken into account. From these broad energy bands, electronic transitions in the energy range from 3.5 eV to 14 eV are possible without significant forbidden energy ranges. As a key result, this demonstrates that the amorphous phase of TiO_2 obeys peculiar optical features that are commonly not observed in the long-range ordered crystalline TiO_2 main phases rutile, anatase, and brookite.

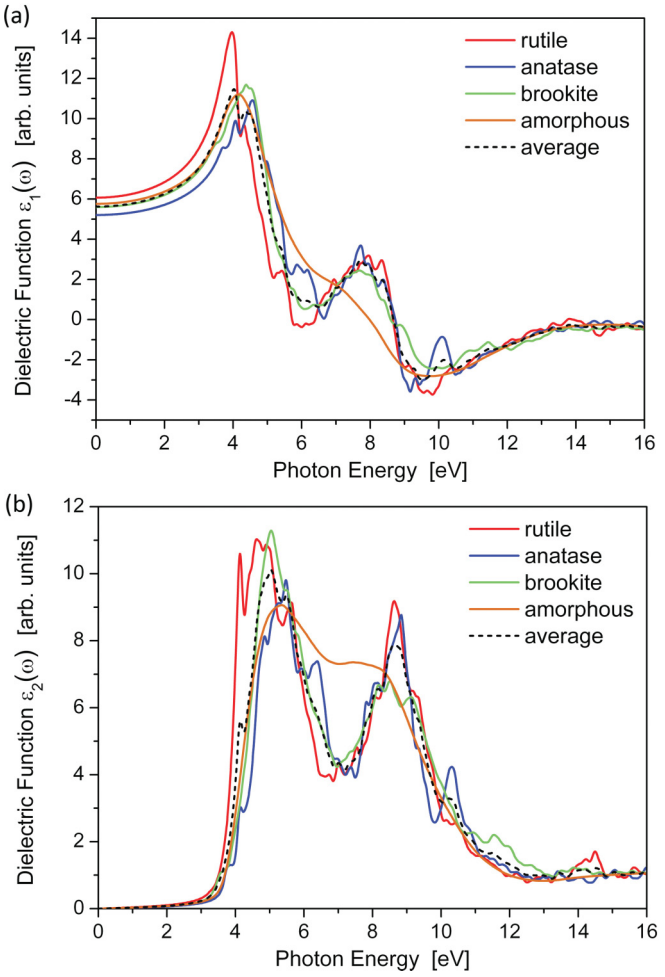

FIG. 11. (Color online) Comparison of the real part $\varepsilon_1(\omega)$ and imaginary part $\varepsilon_2(\omega)$ of the isotropic dielectric function of the crystalline TiO_2 phases rutile, anatase, and brookite and the disordered phase (CPMD + VASP structure) of TiO_2. Also plotted is the equally weighted average of the three crystalline phases.

One interesting observation is related to the phase-averaged dielectric function shown in Fig. 8. Instead of resembling the spectra of a-TiO_2 it is quite close to the brookite phase itself. This indicates a certain similarity between the local atomic environment of orthorhombic brookite and both higher symmetry phases rutile and anatase (see Ref. 17).

G. Optical properties of TiO_2 crystals

So far, we have compared the optical adsorption in a-TiO_2 to the three crystalline main phases rutile, anatase, and brookite. However, most of the existing/fabricable TiO_2 modifications, identified in the extraordinarily rich phase diagram of TiO_2,

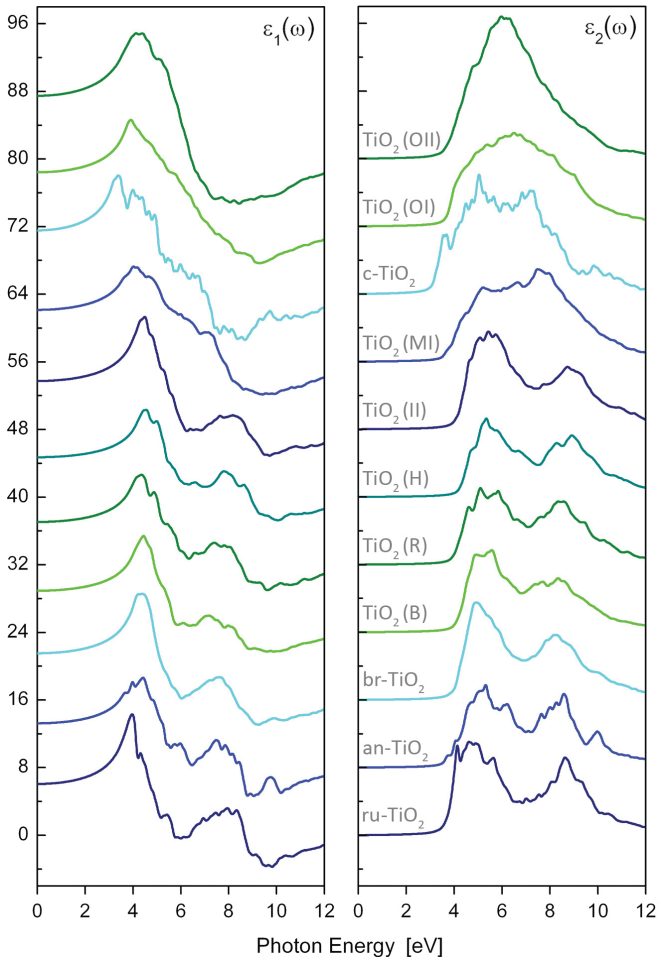

FIG. 12. (Color online) Real and imaginary part of the isotropic dielectric functions of (in ascending order) the crystalline TiO_2 phases rutile (ru-TiO_2), anatase (an-TiO_2), brookite (br-TiO_2), TiO_2(B), TiO_2(R), TiO_2(H), TiO_2(II), TiO_2(MI), c-TiO_2, TiO_2(OI), and TiO_2(OII).

have been ignored so far. In order to identify the additional contributions in the optical spectra of a-TiO_2 it seems natural to extend the investigation to the existing metastable and high-pressure phases. In detail, we have investigated the metastable phases TiO_2(B), TiO_2(R), and TiO_2(H) and the high-pressure phases TiO_2-OI, TiO_2-OII, TiO_2-MI, TiO_2 II, and c-TiO_2. In Fig. 12, the calculated isotropic dielectric functions in IPA are depicted. With exception of 1.2 eV for rutile, a scissors shift of 1.3 eV was applied to all crystalline phases in order to preserve comparability and due to missing experimental band-gap reference data for most phases. From the dielectric functions, it is obvious that all crystalline TiO_2 phases, whose structure is composed from TiO_6 octahedron building bocks, show common optical properties. Especially the characteristic two-peak shape of the imaginary part of the IPA dielectric function, connected to the octahedral-like crystal-field splitting of the unoccupied Ti_{3d} states into e_g and t_{2g} like states, is obvious. Consequently, a change in the local atomic structure, i.e., a Ti ion coordinated by more than 6 O ions, results in a single broad peak in the dielectric function due to the lifting of the octahedral-like symmetry and a continuous first broad conduction band in the electronic DOS. This is comparable to

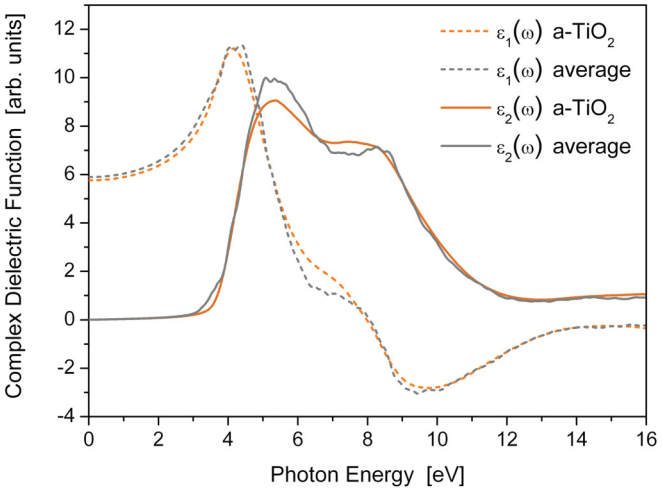

FIG. 13. (Color online) Real and imaginary part of the isotropic dielectric function of a-TiO_2 and the equally weighted averages of the eleven crystalline phases listed in Fig. 12.

the observed continua of electronic states and optical transition energies in the DOS and dielectric function of the amorphous phase. The non-sixfold-coordinated TiO_2 modifications are the four high-pressure phases TiO_2-OI, TiO_2-OII, TiO_2-MI, and c-TiO_2. Out of these, Ti ions are sevenfold coordinated in TiO_2-OI and TiO_2-MI, eightfold coordinated in c-TiO_2, and ninefold coordinated in TiO_2-OII by O ions. As a side note, the reduced band gap of the cubic fluorite phase, reported by various authors,[11,12,137] is reproduced in our data.

In Fig. 13, we have compared the equally weighted average of the dielectric functions of all investigated eleven crystalline phases. Thereby, we assume that the versatile local structure of the amorphous phase reflects a wide cross section of all possible binding situations appearing in the crystalline phases. The obtained crystal-phase average basically reproduces all features of the amorphous phase. The height of the first main peak around 5 eV in the imaginary part is slightly overestimated. However, this discrepancy could probably be further reduced by inclusion of excitonic effects that can have significant influence on the energy region close to the absorption onset, as demonstrated for rutile and anatase. Hence, we emphasize that the amorphous phase of TiO_2 can be understood as a superposition of the diversified local atomic environments (i.e., different types of short-range order) existing in crystalline TiO_2 modofications.

H. Density dependence of the optical response in amorphous TiO_2

In general, electronic properties as the electronic *band* gap and related quantities as the dielectric function should be compared for amorphous and crystalline material phases that approximately share the same mass density. In doing so, the basic influence of density variations does not superimpose the effects of structural disorder. However, an amorphous material modification is not necessarily a disordered phase with a homogeneous mass distribution on an atomic length scale. Commonly, nano- and microstructural inhomogeneities occur in form of voids and formation of grainlike crystallized

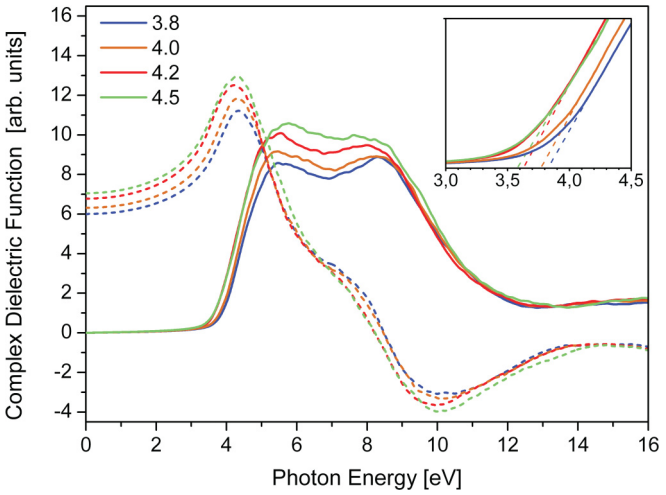

FIG. 14. (Color online) Real (dashed line) and imaginary (solid lines) parts of the isotropic dielectric function $\varepsilon(\omega)$ for a-TiO_2 structure models with mass densities of 3.8, 4.0, 4.2, and 4.5 g/cm^3 obtained using 1632 electronic bands, the Γ points only, and a 1.3 eV scissors shift in all calculations. The inset on the upper right gives a detailed view on the imaginary part of the dielectric function close to the absorption edge.

domains in amorphous samples and have to be considered as sources of local density fluctuations. In order to estimate the extend of linear-response modifications due to variations of the material density, we have generated a series of structure models with different mass densities. All structures were generated by DFTB-MD and successive structural relaxation using VASP.

Figure 14 shows the real and imaginary components of the complex dielectric function for the four mass densities 3.8, 4.0, 4.2, and 4.5 g/cm^3. As a major observation, all four structure models exhibit the same spectral characteristics consisting of the broad absorption band in the energy region from 4 eV to 11 eV. Similar to the structure models investigated up to now, this absorption band still allows the identification of a two-peak substructure which is reminiscent of the e_g and t_{2g} like subband structure of Ti_{3d} conduction states in crystalline TiO_2. With decreasing density, the second subpeak above 7 eV becomes marginally more pronounced than the first subpeak.

From linear extrapolation of the dielectric function (cf. inset in Fig. 14), the energy gap of a-TiO_2 is found to decrease with increasing density. Thereby, the energy gap changes from ∼3.8 to ∼3.6 eV when going from 3.8 to 4.5 g/cm^3. Accordingly, the calculated DFT-PBE HOMO-LUMO-type energy gaps show a decrease from 2.3 eV to 2.06 eV. A band gap decrease with increasing density is also indicted for crystalline TiO_2 by DFT-PBE band gaps of 1.94 eV for anatase (3.8 g/cm^3) and 1.88 eV for rutile (4.2 g/cm^3). The band gap decrease with increasing density is reflected in the real part of the dielectric function by an increase in the dielectric constants in the static limit and across the visible spectral energy range.

In contrast to the differences in the dielectric functions depicted in Fig. 8 that are related to temperature effects and different simulation techniques, changes in the mass density influence the qualitative characteristics of the optical response of a-TiO_2. Especially, the slight change in the spectral-weight distribution of the dielectric function from one subpeak to the other seems to be characteristic to density fluctuations. With increasing density the first subpeak becomes marginally more pronounced than the second. Moreover, the changes in the static dielectric constant are a clear indication for mass-density variations. Neither the numerical simulation technique nor the influence of temperature show a comparable influence on the static and visible-range optical constants.

IV. SUMMARY AND CONCLUSION

From analysis of the static structure factor and the atomic RDFs, we have demonstrated the feasibility of the DFTB and CPMD approach to generate amorphous TiO_2 structures.

The calculated a-TiO_2 (HOMO-LUMO-type) QP gap of ∼3.7 eV for the completely relaxed 4.2 g/cm^3 atomic structures is found to be larger than the QP band gap in rutile and brookite but comparable to anatase. Like for the crystalline phases, the energy states in a-TiO_2 around the fundamental energy gap are formed by occupied $2p$-like states of oxygen and unoccupied $3d$-like states of Ti. The band-tail states that form due to the structural disorder and variations in the local coordination numbers also show the $2p$- and $3d$-like distributions of the electronic charge density. Thereby, states of the more extended valence band tail are located at under-coordinated O ions in Ti_2O building blocks and O ions residing in structural distorted Ti_3O building blocks. The conduction band-tail states represent a superposition of electronic states located at variously coordinated Ti ions in TiO_7,TiO_6, and TiO_5 building blocks. In contrast to octahedrally coordinated TiO_2 crystal phases, neither the density of states nor the dielectric function indicates a distinct crystal field induced splitting of the unoccupied $3d$ states into e_g and t_{2g} like subbands. These differences in the electronic structure occur due to the differences in the local atomic structure. Only ∼50–60 % of the Ti ions still form, partially strongly distorted, TiO_6 polyhedron building blocks. The most important consequence of the loss of local symmetry in a-TiO_2 is the characteristic modification of optical spectra in the energy region from 5 eV to 8 eV.

The DFT-PBE mobility gaps, estimated from an analysis of the localization of electronic states by information entropy based quantities, are at least ∼0.4 eV larger than the DFT-PBE band gaps of the crystalline TiO_2 main phases. The overall size of band tails for occupied and unoccupied states is strongly modified by temperature influences on the atomic structure. While extended band tails result in a significantly reduced HOMO-LUMO-type energy gap for a-TiO_2 structures equilibrated at room temperature, additional structure relaxation increases the energy gap above the calculated band gaps of crystalline TiO_2 polymorphs. Thereby, only a few electronic states within ∼0.1 eV around the band edges show a notable degree of localization for the 0 K equilibrium structure.

In summary, the electronic structure of a-TiO_2 can be characterized as follows: Despite the formal nonvalidity of Bloch's theorem in amorphous solids, the remaining short-range order causes a well-defined separation of bonding and antibonding states separated by an energy gap. Similar to a crystal the small energy differences between various electronic states promote the formation of *band*-type characteristics in the electronic DOS that are comparable to the DOS in TiO_2 crystals. Electronic states close to the *band* edges show

distinct localization characteristics and range into the energy region of the crystal band gap. The tail states emerge from distortions in the local atomic environment of the majority of Ti and accordingly O ions and changes in the local atomic coordination numbers. Similar to defects in crystals, under-coordinated O ions are represented by acceptor like states in the valence tail and over-coordinated Ti ions form donor-like conduction-tail states.

The calculated complex dielectric functions and complex refractive indices of a-TiO_2 are close to the data obtained from various experiments and indicate an optical gap $\lesssim$3.5 eV. Compared to the dielectric function obtained from solution of the BSE, the IPA dielectric functions provide a reasonable basis for analyzing the optical response of a-TiO_2. The inclusion of two-particle excitations mainly accounts for a redshift, while the overall curve characteristics remain qualitatively unchanged. Unfortunately, experimental data on a-TiO_2 are missing in the higher energy range (5–8 eV) that is characterized by stronger absorption/higher oscillator strength as observed for rutile, anatase, and brookite.

The optical-response characteristics are found to be very similar over the whole energy range when changing the mass density from 3.8 to 4.5 g/cm^3, although the energy gap of a-TiO_2 decreases with increasing density.

Since an amorphous TiO_2 phase represents a metastable state, it is reasonable to interpret it as a superposition of the manifold of local atomic configurations that occur in existing crystalline material phases. This explicitly includes crystal phases that normally are unstable under the ambient conditions. Due to inclusion of TiO_2 high-pressure polytypes, the average over eleven crystalline phases allows the reproduction of all spectral features of the a-TiO_2 dielectric function. Such a superposition of crystalline phases could possibly also offer a way for approximately accounting for electron-hole interaction in a-TiO_2 by solving the BSE only for the small unit cells of the various single crystal modifications and avoiding the use of the large unit cells necessary to simulate the disordered material phase.

ACKNOWLEDGMENTS

We thank the Laser Zentrum Hannover e.V. (LZH) for providing us the dielectric function data on ion-beam-sputtered a-TiO_2 films. The calculations were done using grants of computer time from the Regionales Rechenzentrum of the Universität zu Köln (RRZK), the Paderborn Center for Parallel Computing (PC2), and the Höchstleistungs-Rechenzentrum Stuttgart. The Deutsche Forschungsgemeinschaft is acknowledged for financial support. The authors are also grateful to the BMBF, Germany, for financial support in terms of the PluTO-grant to promote modern optical technologies.

[1] R. Marchand, L. Brohan, and M. Tournoux, Mater. Res. Bull. **15**, 1129 (1980).
[2] J. F. Banfield and D. R. Veblen, Am. Mineral. **77**, 545 (1992).
[3] M. Latroche, L. Brohan, R. Marchand, and M. Tournoux, J. Solid State Chem. **81**, 78 (1989).
[4] J. Akimoto, Y. Gotoh, Y. Oosawa, N. Nonose, T. Kumagai, K. Aoki, and H. Takei, J. Solid State Chem. **113**, 27 (1994).
[5] P. Y. Simons and F. Dachille, Acta Cryst. **23**, 334 (1967).
[6] J. Haines and J. M. Léger, Physica B **192**, 233 (1993).
[7] K. Lagarec and S. Desgreniers, Solid State Commun. **94**, 519 (1995).
[8] H. Sato, S. Endo, M. Sugiyama, T. Kikegawa, O. Shimomura, and K. Kusaba, Science **251**, 786 (1991).
[9] N. A. Dubrovinskaia, L. S. Dubrovinsky, R. Ahuja, V. B. Prokopenko, V. Dmitriev, H. P. Weber, J. M. Osorio-Guillen, and B. Johansson, Phys. Rev. Lett. **87**, 275501 (2001).
[10] L. S. Dubrovinsky, N. A. Dubrovinskaia, V. Swamy, J. Muscat, N. M. Harrison, R. Ahuja, B. Holm, and B. Johansso, Nature (London) **410**, 653 (2001).
[11] M. Mattesini, J. S. de Almeida, L. Dubrovinsky, N. Dubrovinskaia, B. Johansson, and R. Ahuja, Phys. Rev. B **70**, 212101 (2004).
[12] D. Y. Kim, J. S. de Almeida, L. Koči, and R. Ahuja, Appl. Phys. Lett. **90**, 171903 (2007).
[13] X. Wu, E. Holbig, and G. Steinle-Neumann, J. Phys.: Condens. Matter **22**, 295501 (2010).
[14] I. Manzini, G. Antonioli, D. Bersani, P. P. Lottici, G. Gnappi, and A. Montenero, J. Non. Cryst. Sol., **192** 519 (1995); **193** 519 (1995).
[15] V. Petkov, G. Holzhüter, U. Tröge, Th. Gerber, and B. Himmel, J. Non-Crystal. Sol. **231**, 17 (1998).
[16] D. Reyes-Coronado, G. Rodríguez-Gattorno, M. E. Espinosa-Pesqueira, C. Cab, R. de Coss, and G. Oskam, Nanotechnology **19**, 145605 (2008).
[17] M. Landmann, E. Rauls, and W. G. Schmidt, J. Phys.: Condens. Matter **24**, 195503 (2012).
[18] J. M. Verduzco, H. Chung, C. Hu, and W. Choe, Inorg. Chem. **48**, 9060 (2009).
[19] K. Hashimoto, H. Irie, and A. Fujishima, AAPPS Bulletin **17**, 12 (2007).
[20] A. Fujishima, X. Zhang, and D. A. Tryk, Surf. Sci. Rep. **63**, 515 (2008).
[21] L. S. Hsu, R. Rujkorakarn, J. R. Sites, and C. Y. She, J. Appl. Phys. **59**, 3475 (1986).
[22] X. Chen and S. S. Mao, Chem. Rev. **107**, 2891 (2007).
[23] H. Zhang, B. Chen, J. F. Banfield, and G. A. Waychunas, Phys. Rev. B **78**, 214106 (2008).
[24] S. B. Amor, G. Baud, J. P. Besse, and M. Jacquet, Mater. Sci. Eng. B **47**, 110 (1997).
[25] R. Dannenberg and P. Greene, Thin Sol. Films **360**, 122 (2000).
[26] S. B. Amor, L. Guedri, G. Baud, M. Jacquet, and M. Ghedira, Mat. Chem. Phys. **77**, 903 (2002).
[27] D. Mardare and G. I. Rusu, Mat. Lett. **56**, 210 (2002).
[28] K. Eufinger, D. Poelman, H. Poelman, R. De Gryse, and G. B. Marin, Appl. Surf. Sci. **254**, 148 (2007).
[29] E. Gofuku, Y. Toyoda, Y. Uehara, M. Kohara, and M. Nunoshita, Appl. Surf. Sci. **48**, 343 (1991); **49**, 343 (1991).

[30] S. Y. Kim, Appl. Optics **35**, 6703 (1996).
[31] H. Takikawa, T. Matsui, T. Sakakibara, A. Bendavid, and P. J. Martin, Thin Sol. Films **348**, 145 (1999).
[32] Z. W. Zhao, B. K. Tay, S. P. Lau, and G. Q. Yu, J. Cryst. Growth **268**, 543 (2004).
[33] V. Luca, S. Djajanti, and R. F. Howe, J. Phys. Chem. B **102**, 10650 (1998).
[34] Z. Wang, U. Helmersson, and P.-O. Käll, Thin Sol. Films **405**, 50 (2002).
[35] D. Mardare and P. Hones, Mater. Sci. Eng. B **68**, 42 (1999).
[36] M. Zhang, G. Lin, C. Dong, and L. Wen, Surf. & Coat. Technol. **201**, 7252 (2007).
[37] J. Nowotny, T. Bak, T. Burg, M. K. Nowotny, and L. R. Sheppard, J. Phys. Chem. C **111**, 9769 (2007).
[38] D. Sarkar, C. K. Ghosh, U. N. Maiti, and K. K. Chattopadhyay, Physica B **406**, 1429 (2011).
[39] H. Zhang, J. F. Banfield, and L. Wen, J. Mater. Chem. **8**, 2073 (1998).
[40] M. Fernández-García, C. Belver, Jonathan C. Hanson, Xianqin Wang, and J. A. Rodriguez, J. Am. Chem. Soc. **129**, 13604 (2007).
[41] S. Bauer, A. Pittrof, H. Tsuchiya, and P. Schmuki, Electrochem. Commun. **13**, 538 (2011).
[42] E. Leitão, R. A. Silva, and M. A. Barbosa, Corros. Sci. **39**, 377 (1996).
[43] R. Karpagavalli, A. Zhou, P. Chellamuthu, and K. Nguyen, J. Biomed. Mater. Res. Part A **83**, 1087 (2007).
[44] K. M. Glassford and J. R. Chelikowsky, Phys. Rev. B **46**, 1284 (1992).
[45] P. J. Hardman, G. N. Raikar, C. A. Muryn, G. van der Laan, P. L. Wincott, G. Thornton, D. W. Bullett, and P. A. D. M. A. Dale, Phys. Rev. B **49**, 7170 (1994).
[46] S.-D. Mo and W. Y. Ching, Phys. Rev. B **51**, 13023 (1995).
[47] M. Mikami, S. Nakamura, O. Kitao, H. Arakawa, and X. Gonze, Jpn. J. Appl. Phys. **39**, L847 (2000).
[48] R. Asahi, Y. Taga, W. Mannstadt, and A. J. Freeman, Phys. Rev. B **61**, 7459 (2000).
[49] M. Calatayud, P. Mori-Sánchez, A. Beltrán, A. M. Pendás, E. Francisco, J. Andrés, and J. M. Recio, Phys. Rev. B **64**, 184113 (2001).
[50] J. Muscat, V. Swamy, and N. M. Harrison, Phys. Rev. B **65**, 224112 (2002).
[51] C. Qiang and C. Hong-Hong, Chin. Phys. **13**, 2121 (2004).
[52] Y. Jing-Xin, F. Min, J. Guang-Fu, and C. Xiang-Rong, Chin. Phys. B **18**, 269 (2009).
[53] F. M. Hossain, L. Sheppard, J. Nowotny, and G. E. Murch, J. Phys. Chem. Sol. **69**, 1820 (2008).
[54] E. Shojaee and M. R. Mohammadizadeh, J. Phys.: Condens. Matter **22**, 015401 (2010).
[55] A. F. da Silva, I. Pepe, C. S. S. Brasil, D. G. F. David, E. F. da Silva Jr., C. Persson, T. Lindgren, J. S. de Almeida, C. M. Araújo, and R. Ahuja, Phys. Status Solidi C **1**, S241 (2004).
[56] C. Persson and A. F. da Silva, Appl. Phys. Lett. **86**, 231912 (2005).
[57] F. Thomazi, L. S. Roman, A. F. da Silva, and C. Persson, Phys. Status Solidi C **6**, 2740 (2009).
[58] L. K. Dash, F. Bruneval, V. Trinité, N. Vast, and L. Reining, Comput. Mater. Sci. **38**, 482 (2007).
[59] H. M. Lawler, J. J. Rehr, F. Vila, S. D. Dalosto, E. L. Shirley, and Z. H. Levine, Phys. Rev. B **78**, 205108 (2008).
[60] L. Chiodo, J. M. García-Lastra, A. Iacomino, S. Ossicini, J. Zhao, H. Petek, and A. Rubio, Phys. Rev. B **82**, 045207 (2010).
[61] A. Thilagam, D. J. Siompson, and A. R. Gerson, J. Phys.: Condens. Matter **23**, 025901 (2011).
[62] W. Kang and M. S. Hybertsen, Phys. Rev. B **82**, 085203 (2010).
[63] U. Diebold, Surf. Sci. Rep. **48**, 53 (2003).
[64] U. Diebold, N. Ruzycki, G. S. Herman, and A. Selloni, Catalysis Today **85**, 93 (2003).
[65] X.-Q. Gong and A. Selloni, Phys. Rev. B **76**, 235307 (2007).
[66] A. Selloni, Nat. Mater. **7**, 613 (2008).
[67] X.-Q. Gong, N. Khorshidi, A. Stierle, V. Vonk, C. Ellinger, H. Dosch, H. Cheng, A. Selloni, Y. He, O. Dulub, and U. Diebold, Surf. Sci. **603**, 138 (2009).
[68] M. D. Rasmussen, L. M. Molina, and B. Hammer, J. Chem. Phys. **120**, 988 (2004).
[69] S. Wendt, R. Schaub, J. Matthiesen, E. K. Vestergaard, E. Wahlström, M. D. Rasmussen, P. Thostrup, L. M. Molina, E. Lægsgaard, I. Stensgaard, B. Hammer, and F. Besenbacher, Surf. Sci. **598**, 226 (2005).
[70] U. Martinez and B. Hammer, J. Chem. Phys. **134**, 194703 (2011).
[71] P. W. Anderson, Phys. Rev. **109**, 1492 (1958).
[72] P. W. Anderson, Phys. Rev. Lett. **34**, 953 (1975).
[73] M. H. Cohen, H. Fritzsche, and S. R. Ovshinsky, Phys. Rev. Lett. **22**, 1065 (1969).
[74] Sir N. Mott, Rev. Mod. Phys. **50**, 203 (1978).
[75] B. Prasai, B. Cai, D. A. Drabold, M. K. Underwood, and J. P. Lewis, *MS&T-11 Conf. Proceedings* (Curran Associates, Inc., New York, 2011).
[76] V. van Hoang, Phys. Status Solidi B **244**, 1280 (2007).
[77] Bokhimi, A. Morales, O. Novaro, T. López, E. Sánchez, and R. Gómez, J. Mater. Res. **10**, 2788 (1995).
[78] P. Hohenberg and W. Kohn, Phys. Rev. **136**, B864 (1964).
[79] W. Kohn and L. J. Sham, Phys. Rev. **140**, A1133 (1965).
[80] P. E. Blöchl, Phys. Rev. B **50**, 17953 (1994).
[81] G. Kresse and D. Joubert, Phys. Rev. B **59**, 1758 (1999).
[82] G. Kresse and J. Furthmüller, Comput. Mater. Sci. **6**, 15 (1996).
[83] J. P. Perdew and K. Burke and M. Ernzerhof, Phys. Rev. Lett. **77**, 3865 (1996).
[84] J. Heyd, G. E. Scuseria, and M. Ernzerhof, J. Chem. Phys. **118**, 8207 (2003).
[85] J. Heyd and G. E. Scuseria, J. Chem. Phys. **121**, 1187 (2004).
[86] J. Heyd, J. E. Peralta, G. E. Scuseria, and R. L. Martin, J. Chem. Phys. **123**, 174101 (2005).
[87] J. Heyd, G. E. Scuseria, and M. Ernzerhof, J. Chem. Phys. **124**, 219906 (2006).
[88] L. Hedin, Phys. Rev. **139**, A796 (1965).
[89] L. Hedin and S. Lundqvist, in *Solid State Physics*, edited by F. Seitz, D. Turnbull, and H. Ehrenreich (Academic Press, New York, 1970), Vol. 23, p. 1.
[90] M. Shishkin and G. Kresse, Phys. Rev. B **74**, 035101 (2006).
[91] M. Shishkin and G. Kresse, Phys. Rev. B **75**, 235102 (2007).
[92] F. Fuchs, J. Furthmüller, F. Bechstedt, M. Shishkin, and G. Kresse, Phys. Rev. B **76**, 115109 (2007).
[93] M. Shishkin, M. Marsman, and G. Kresse, Phys. Rev. Lett. **99**, 246403 (2007).
[94] C. Mietze, M. Landmann, E. Rauls, H. Machhadani, S. Sakr, M. Tchernycheva, F. H. Julien, W. G. Schmidt, K. Lischka, and D. J. As, Phys. Rev. B **83**, 195301 (2011).

[95]L. J. Sham and T. M. Rice, Phys. Rev. **144**, 708 (1966).
[96]W. Hanke and L. J. Sham, Phys. Rev. B **12**, 4501 (1975).
[97]W. Hanke and L. J. Sham, Phys. Rev. B **21**, 4656 (1980).
[98]S. Albrecht, L. Reining, R. Del Sole, and G. Onida, Phys. Rev. Lett. **80**, 4510 (1998).
[99]W. G. Schmidt, S. Glutsch, P. H. Hahn, and F. Bechstedt, Phys. Rev. B **67**, 085307 (2003).
[100]M. Elstner, D. Porezag, G. Jungnickel, J. Elsner, M. Haugk, T. Frauenheim, S. Suhai, and G. Seifert, Phys. Rev. B **58**, 7260 (1998).
[101]D. Porezag, T. Frauenheim, T. Köhler, G. Seifert, and R. Kaschner, Phys. Rev. B **51**, 12947 (1995).
[102]Th. Frauenheim, G. Seifert, M. Elstner, Z. Haynal, G. Jungnickel, S. Suhai, and R. Scholz, Phys. Status Solidi B **227**, 41 (2000).
[103]Y. Lifshitz, Th. Köhler, Th. Frauenheim, I. Guzmann, A. Hoffman, R. Q. Zhang, X. T. Zhou, and S. T. Lee, Science **297**, 1531 (2002).
[104]G. Seifert, Th. Köhler, and Th. Frauenheim, Appl. Phys. Lett. **77**, 1313 (2000).
[105]R. Car and M. Parrinello, Phys. Rev. Lett. **55**, 2471 (1985).
[106]G. Dolgonos, B. Aradi, N. H. Moreira, and Th. Frauenheim, J. Chem. Theory Comput. **6**, 266 (2010).
[107]K. M. Glassford, N. Troullier, José Luis Martins, and J. R. Chelikowsky, Solid State Commun. **76**, 653 (1990).
[108]S. Langel, W. Surf. Sci **496**, 141 (2002).
[109]A. D. Becke, Phys. Rev. A **38**, 3098 (1988).
[110]C. N. J. Wagner, J. Non.-Cryst. Sol. **31**, 1 (1978).
[111]K. S. Vahvaselkä, Phys. Status Solidi A **72**, 261 (1982).
[112]A. V. Krukau, O. A. Vydrov, A. F. Izmaylov, and G. E. Scuseria, J. Chem. Phys. **125**, 224106 (2006).
[113]H. Ehrenreich and M. H. Cohen, Phys. Rev. **115**, 786 (1959).
[114]A. Rényi, in *Proceedings of the Fourth Berkeley Symposium on Mathematical Statistics and Probability*, edited by J. Neyman (University of California Press, Berkeley, 1961), Vol. 1, p. 547.
[115]K. Życzkowski, Open Sys. Information Dyn. **10**, 297 (2003).
[116]C. E. Shannon, Bell Syst. Tech. J. **27**, 379 (1948).
[117]C. E. Shannon, Bell Syst. Tech. J. **30**, 50 (1951).
[118]The information entropy based quantity $W(\lambda)$ was applied by Lewis *et al*. (Refs. 119 and 120) to investigate the localization of electronic states in a DNA double-helix model.
[119]J. P. Lewis, J. Pikus, T. E. Cheatham, III, E. B. Starikov, H. Wang, J. Tomfohr, and O. F. Sankey, Phys. Status Solidi B **233**, 90 (2002).
[120]J. P. Lewis, T. E. Cheatham, III, E. B. Starikov, H. Wang, and O. F. Sankey, J. Phys. Chem. B **107**, 2581 (2003).
[121]B. Mirbach and H. J. Korsch, Ann. Phys. **265**, 80 (1998).
[122]R. Atta-Fynn, P. Biswas, P. Ordejón, and D. A. Drabold, Phys. Rev. B **69**, 085207 (2004).
[123]The IPR was used by Atta-Fynn *et al*. (Ref. 122) to investigate electronic localization in amorphous hydrogenated Si (a-Si:H). Recently Cai *et al*. (Ref. 124) investigated localized states in the electronic structure of amorphous GaN.
[124]B. Cai and D. A. Drabold, Phys. Rev. B **84**, 075216 (2011).
[125]P. Sorantin and K. Schwarz, Inorg. Chem. **31**, 567 (1992).
[126]B. Jiang, J. M. Zuo, N. Jiang, M. O'Keeffe, and J. C. H. Spence, Acta Cryst. Mater. A **59**, 341 (2003).
[127]J. D. DeLoach, G. Scarel, and C. R. Aita, J. Appl. Phys. **85**, 2377 (1999).
[128]J. Tauc, R. Grigorovici, and A. Vancu, Phys. Status Solidi **15**, 627 (1966).
[129]J. Tauc, A. Menth, and D. L. Wood, Phys. Rev. Lett. **25**, 749 (1970).
[130]J. Tauc (ed.), *Amorphous and Liquid Semiconductors* (Plenum Press, London, 1974).
[131]P. Kubelka and F. Munk, Zeitschrift für technische Physik **12**, 593 (1931).
[132]P. Kubelka, J. Opt. Soc. Am. **38**, 448 (1948).
[133]M. Turowski, H. Ehlers, and D. Ristau, Laser Zentrum Hannover e.V. (LZH) (unpublished).
[134]Y. Yamada, H. Uyama, T. Murata, and H. Nozoye, J. Vac. Sci. Technol. A **19**, 2479 (2001).
[135]M. H. Suhail, G. M. Rao, and S. Mohan, J. Appl. Phys. **71**, 1421 (1992).
[136]G. Lucovsky, J. Optoelectron. Adv. Mater. **3**, 155 (2001).
[137]X. G. Kong, Y. Yu, and T. Gao, Euro Phys. J. B **76**, 365 (2010).